



**João Filipe Tapadinhas Puga Leal**

Licenciado em Ciências de Engenharia Electrotécnica e de Computadores

## **Optimization of Ring Oscillators**

Dissertação para obtenção do Grau de Mestre em Engenharia Electrotécnica e de Computadores

Orientador: Maria Helena Silva Fino, Professora Auxiliar,  
Faculdade de Ciências e Tecnologia da Universidade  
Nova de Lisboa

Júri:

Presidente: Prof. Doutor Fernando José Almeida Vieira do Coito  
Arguente: Prof. Doutor Luís Augusto Bica Gomes de Oliveira  
Vogal: Prof. Doutora Maria Helena Silva Fino



## **Optimization of Ring Oscillators**

Copyright © João Filipe Tapadinhas Puga Leal, FCT/UNL e UNL

A Faculdade de Ciências e Tecnologia e a Universidade Nova de Lisboa têm o direito, perpétuo e sem limites geográficos, de arquivar e publicar esta dissertação através de exemplares impressos reproduzidos em papel ou de forma digital, ou por qualquer outro meio conhecido ou que venha a ser inventado, e de a divulgar através de repositórios científicos e de admitir a sua cópia e distribuição com objectivos educacionais ou de investigação, não comerciais, desde que seja dado crédito ao autor e editor.



## Acknowledgements

I am deeply grateful to my supervisor, Prof. Helena Fino, whose devoted scientific supervision made possible this thesis. Her scientific knowledge, along with her support and encouragement, were always present throughout thesis development. I cannot express how grateful I am for such effort and friendship. Thank you very much.

To my father, for his friendship, guidance and his always present support, persistence and help with every mean he has at his reach. To my mother, to my sister, to my girlfriend and all my family, for being always a source of love, support and encouragement.

The last but not the least, to all my colleagues and friends who helped me by contributing with ideas, support and knowledge, throughout this work.



## Resumo

Os osciladores controlados por tensão são, de todos os blocos constituintes dos PLLs, aqueles cuja implementação é mais crítica, uma vez que estes blocos são responsáveis pela geração de sinal de saída. Os VCOs podem ser implementados tendo por base osciladores LC ou osciladores em anel. Os osciladores em anel, não obstante serem piores do ponto de vista de ruído de fase, são preferencialmente usados por ocuparem menor área e apresentarem uma maior gama de sintonia.

O trabalho proposto nesta dissertação tem por objectivo o desenvolvimento de um ambiente para dimensionamento automático de osciladores controlados por tensão com topologia em anel. Neste trabalho considerou-se uma metodologia de projeto baseada em otimização com recurso a um modelo analítico do oscilador. O modelo do oscilador tem por base o modelo EKV na caracterização dos transístores, por forma a garantir a sua aplicabilidade a tecnologias de dimensões submicrométricas.

O trabalho desenvolvido decorreu de acordo com as seguintes fases:

- Estudo de osciladores em anel e de modelos propostos na literatura
- Avaliação das limitações dos modelos existentes e proposta de utilização do modelo EKV.
- Determinação automática dos parâmetros do modelo EKV para a tecnologia UMC-130
- Desenvolvimento de modelo analítico para caracterização de VCO com célula de atraso pré-definida.
- Utilização de técnicas de otimização no dimensionamento automático de VCOs

**Palavras chave:** VCOs, Osciladores em Anel, Ruído de Fase, Otimização





## Abstract

Voltage Controlled Oscillators (VCOs) are from all the building blocks of a PLL, those whose implementation is more critical, since the quality of the signal depends on its performance. The VCOs can be implemented based on LC oscillators or ring oscillators. The ring oscillators, despite of being worst when it comes to manners of phase noise, they are rather used due to lower power consumption, wider tuning range and occupying less area.

Despite the fact that VCOs are widely used in last years, their designed is still a problem hard to deal with, since the ring oscillators circuits must satisfy some specifications such as area, power, speed and noise.

The work proposed in this thesis aims at the development of an environment for automatic scaling of voltage-controlled oscillators with ring topology. In this work it was considered a design methodology based optimization using an analytical model of the oscillator. The oscillator model is based on the EKV model for the characterization of the transistors so as to ensure its applicability to submicron dimensions technologies.

The work took place according to the following phases:

- Study of ring oscillators and models proposed in the literature
- Evaluation of the limitations of existing models and proposed use of EKV model.
- Automatic determination of the parameters of the EKV model for UMC130 technology
- Development of an analytic model for characterizing the VCO with predefined delay cell.
- Use of optimization techniques for automatic sizing of the VCOs

**Keywords:** VCOs, Ring Oscillator, Phase-Noise, Optimization



## Table of Contents

Acknowledgements .....	i
Resumo .....	vii
Abstract .....	ix
List of Figures .....	xiii
List of Tables.....	xv
List of Abbreviations.....	xvii
1. Introduction .....	1
1.1. Introduction .....	1
1.2. Thesis Organization.....	2
1.3. Main Contributions.....	3
2. Voltage Controlled Oscillators .....	5
2.1. Introduction .....	5
2.2. Oscillators Topologies.....	5
2.2.1. LC Oscillators.....	5
2.2.2. Ring VCOs .....	7
2.2.3. Simple Inverter .....	8
2.2.4. Differential Inverters .....	9
2.3. Ring VCO Automatic Design.....	11
2.4. Working Example and Results .....	14
2.5. Conclusions .....	15
3. EKV Models.....	17
3.1. Introduction .....	17
3.2. The EKV Model .....	17
3.2.1. Weak inversion.....	21
3.2.2. Drain Current.....	21
3.3. Parameters Extraction.....	24
3.3.1. Drain Current.....	24
3.3.2. Extraction of <i>I<sub>specific</sub></i> .....	24
3.3.3. The Pinch-off Voltage .....	26
3.3.4. Automatic Generation of the EKV Model Parameters .....	30
3.4. Work Examples .....	31
3.4.1. Single Inverter .....	31
3.4.2. Three Stages Inverter.....	32

3.5.	Conclusions.....	33
4.	Project of a VCO with EKV Model .....	35
4.1.	Introduction.....	35
4.2.	Ring VCO Design Considerations .....	35
4.2.1.	Bias Stage.....	37
4.2.2.	Effective Capacitance .....	38
4.3.	Optimization of Ring VCOs .....	41
5.	Conclusions.....	45
5.1.	Conclusions.....	45
5.2.	Future Work .....	47
6.	Bibliography .....	49
	Annex I .....	51
	Annex II .....	55

## List of Figures

Figure 2.1- Ring Oscillator Structure.....	7
Figure 2.2- Ring Oscillator with simple inverter cells .....	8
Figure 2.3- Differential Delay Ring .....	9
Figure 2.4- Maneatis d symmetric load delay cell .....	9
Figure 2.5- Frequency Response of the VCO .....	14
Figure 3.1- Cross section of an idealized n-channel MOS transistor, with definitions of both voltage and current.....	18
Figure 3.2- Pinch-off voltage and slope factor as function of the gate voltage.....	20
Figure 3.3- Inversion charge as a function of the channel potential .....	22
Figure 3.4- A - Circuit configuration for specific current extraction. $W=50\mu$ , $L=10\mu$ ; B - Root ( $I_d$ ) vs $V_s$ characteristic.....	25
Figure 3.5- A- Circuit for measuring the $V_p$ vs $V_g$ characteristic ; B- $V_p$ vs $V_g$ characteristic. 26	
Figure 3.6- Estimated vs Simulated results from $V_p$ vs $V_g$ characteristic. Nmos: $W=50\mu$ , $L=10\mu$ . Pmos: $W=10\mu$ , $L=1\mu$ .....	28
Figure 3.7- WETA and LETA Pmos extraction from $V_p$ vs $V_g$ characteristic .....	28
Figure 3.8 Estimated (red) vs Simulated (blue) current of an Nmos and Pmos respectively.....	29
Figure 3.9- Estimated vs Simulated output for one stage inverter. Nmos: $W=20\mu$ , $L=5\mu$ . Pmos: $W=80\mu$ , $L=20\mu$ .....	31
Figure 3.10- Three Stage Inverter Configuration. Nmos: $W=20\mu$ , $L=5\mu$ . Pmos: $W=80\mu$ , $L=10\mu$ .....	32
Figure 3.11- Estimated vs Simulated output for a three stage inverter .....	32
Figure 4.1- Maneatis cell and Bias Current Source.....	36
Figure 4.2- Frequency vs $V_c$ characteristic of the 7 stages R-VCO for different sizes of the bias transistors .....	37



## List of Tables

Table 2.1- Transistor Sizes for the working example .....	14
Table 3.1- Operating Regions of a EKV transistor, with respect to the surface potential .....	18
Table 3.2 Nmos transistor Parameters.....	29
Table 3.3 Pmos transistor Parameters .....	29
Table 3.4 Model vs Simulation delays and relative error.....	33
Table 4.1- Capacitance simulated vs Capacitance estimated .....	39
Table 4.2 Frequency simulated vs Frequency estimated.....	39
Table 4.3 Transistors sizes optimization .....	41
Table 4.4- Frequency estimated against frequency simulated for a 7 stage Ring VCO.....	42
Table 4.5- Frequency estimated against frequency simulated for a 5 stage Ring VCO.....	42
Table 4.6- Frequency estimated against frequency simulated for a 3 stage Ring VCO.....	42





## List of Abbreviations

**PLL**      **P**hase **L**ocked **L**oop

**VCO**      **V**oltage **C**ontrolled **O**scillator

**RO**        **R**ing **O**scillators

**CMOS**    **C**omplementary **M**etal-**O**xide-**S**emiconductor

**NMOS**    **N**channel **M**etal-**O**xide-**S**emiconductor

**PMOS**    **P**channel **M**etal-**O**xide-**S**emiconductor

**MOSFET** **M**osfet-**O**xide-**S**emiconductor **F**ield-**E**ffect **T**ransistor

**RF**        **R**adio **F**requency

**W/L**      **W**idth/**L**ength



## 1. Introduction

### 1.1. Introduction

The exponential evolution of the technology towards nanometer sizes during the past years yielded an incredible development in applications of electronic devices, such as in wireless mobile communications. As result of the progress in technology development, and the use of deep submicron CMOS processes, digital circuits have become faster, more precise, and with decreased of the implementation area. This evolution, however, has not been directly observed in analog/RF circuits where the need for having circuits operating at higher frequencies, with reduced power supply voltages (for low power consumption) and implemented with deep sub-micrometric technologies is still a challenge task for the designers. As a matter of fact, designers must take into account that deep submicron technologies lead to an increase in parasitic capacitances due to the reduction of the oxide thickness. Furthermore, regarding MOSFET transistors new non-ideal effects, arising mainly due to the very small dimensions of the transistor channel, make the usually transistor models quite inaccurate.

The implementation of wireless transceivers has driven the need for integrated, low power frequency synthesizers. Frequency synthesizers provide the precise reference frequencies for modulation and demodulation of RF signals. These frequency synthesizers are implemented with Voltage Controlled Oscillators (VCOs).

Fully integrated VCOs may be implemented either using a ring topology or with an LC topology. Although the technological evolution has permitted the implementation of fully integrated inductors, their quality factor is still a bottleneck in what concerns their use for the implementation of VCOs for RF frequency range. Higher quality inductors may be obtained at the expense of larger areas of implementation, thus compromising the trend for implementing circuits in the smallest area possible. Ring VCOs, on the other hand, are known for being easily integrated in standard CMOS technologies. They also show a wide tuning range and if implemented with a small number of stages they occupy less area than LC-VCOS.

In spite of the widespread use both in communication circuits and in microprocessors, no systematic efficient methodology for designing ring VCOs is adopted by designers. Traditionally the design of a VCO starts with the choice of the number of stages for a desired oscillation frequency. Then a final tuning of the results is performed through iterative simulations. This

approach, however, is a time consuming prohibitive process because transient circuit simulations must be run long enough before steady state is attained. Furthermore, as new standards for communications are imposing ever more stringent specifications both in terms of frequency of operation and phase-noise characteristics, optimization based design methodologies are becoming more popular.

With the aim of increasing the efficiency in the design process, accurate models for the evaluation of the delay introduced by each stage have been proposed in the literature [2, 3]. Although several models have been proposed, their accuracy is hindered by the use of the generally adopted quadratic law for the characterization of MOSFETs in saturation region of operation. During the last decade new models have been proposed for Ring VCOs using submicron technologies [4, 5]. Yet the necessity for integrating the VCO model into an optimization loop makes the EKV Mosfet model a best candidate for characterizing the devices behavior, since only one expression is valid for all regions of operation and from weak inversion till strong inversion.

In this work the EKV model will be used for deriving the analytical characterization of Ring VCOs.

## **1.2. Thesis Organization**

This thesis focuses on the use of optimization techniques in the design of ring oscillators, using the EKV Model, in order to ensure a minimization of phase noise, and hence reduce the main disadvantage of this type of oscillators when compared to LC oscillators. Chapter 2 provides an introduction to the Voltage Controlled Oscillators (VCOs) along with the main VCO topologies, a presentation of the Mead delay cell used in the proposed model as well as an illustration of the limitation of the proposed models when applied for deep-submicron technologies. Chapter 3 is dedicated to the use of the EKV Model for the characterization of transistors in deep-submicron technologies, where a detailed description of the methodology adopted for the determination of the model parameters for the UMC130 technology and their validation is presented. The Chapter 4 addresses to the optimization-based design of Nmos symmetric load ring VCOs, where a new model for its characterization as well as its validation is presented. Finally Chapter 5 concludes the thesis with an analysis to the results obtained and future research directions.

### 1.3. Main Contributions

The work developed considers the following contributions:

- Implementation in Matlab of a script for the automatic generation of EKV parameter models for both NMOS and PMOS parameters for the UMC130 Technology
- Implementation in Matlab of a script for implementing EKV model for both NMOS and PMOS Transistors for the UMC130 Technology.
- Implementation in Matlab of a script for the automatic generation of ring VCO frequency vs control voltage response, using the EKV model.
- Integration of the ring VCO model in an optimization-based environment for the design of Ring VCOs



## **2. Voltage Controlled Oscillators**

### **2.1. Introduction**

In this chapter an introduction to Voltage Controlled Oscillator will be presented. The main VCO topologies used for RF applications are briefly described, and then the ring Voltage controlled oscillators are addressed in more detail. After introducing the single-ended oscillator, the differential oscillator with the Maneatis delay cell is presented [6]. The models proposed in the literature for the Maneatis based differential ring oscillator are presented. Finally, the limitation of the proposed models when applied for deep-submicron technologies UMC-130 is illustrated.

### **2.2. Oscillators Topologies**

Typically, the VCOs are designed based on two different approaches, Ring Oscillators (RO) and the LC Oscillators. Although LC VCOs offer much better phase-noise performance when compared to Ring VCOs, they usually show a narrower tuning range. Furthermore the necessity for using fully integrated spiral inductors leads to implementations with larger area. Ring based VCOs on the other hand present larger tuning range, smaller layout area and lower power consumption. Therefore, a Ring VCO based PLL is usually considered first due to its design simplicity and cost effectiveness. On this chapter, a short introduction as well as a presentation of some basic designs associated to each approach will be made.

#### **2.2.1. LC Oscillators**

LC Oscillators are often used in radio frequency circuits, when high frequency is required, due to their low noise phase. This type of oscillators use as filter in the feedback loop, LC resonant circuits to set the operating frequency, consisting of an inductor (L) and a capacitor (C) connected together. An LC circuit can store electrical energy oscillating at its resonant frequency, when charge flows back and forth between the capacitor's plates through the inductor. The resonant effect happens when the inductive and capacitive reactance are equal in magnitude and cancel out each other, leaving only the resistance of the circuit to oppose the flow of the current, meaning that there is no phase shift as the current is in phase with the voltage.

The frequency of oscillation is determined by the inductive and capacitance values through the following expression:

$$f_0 = \frac{\omega_0}{2\pi} = \frac{1}{2\pi \cdot \sqrt{LC}} \quad (2.1)$$

The main disadvantage of these oscillators for RF frequencies consists on the difficulty of implementing integrated inductors with high quality factor.



### 2.2.2. Ring VCOs

The RO designed with a chain of delay stages have generated great interest due to their numerous useful features[7]:

- i. Easily design with the state-of-art integrated circuit;
- ii. Can achieve its oscillations at a low voltage;
- iii. Provide high frequency oscillations with dissipating low power;
- iv. Can be electrically tuned;
- v. Can provide wide tuning range;
- vi. Can provide multiphase outputs because of their basic structure.

RO is a cascaded combination of an n number of delay stages, connected in close loop chain, whose output oscillates between two voltage levels. A RO only requires power to operate, above a certain threshold voltage the oscillations begin spontaneously. To achieve self-sustained oscillation, the ring must provide a phase shift of  $2\pi$  and have unity voltage gain at the frequency of oscillation[8].

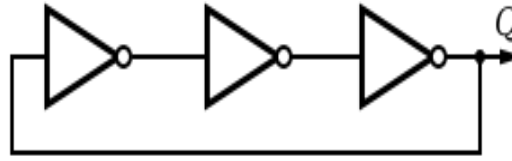


Figure 2.1- Ring Oscillator Structure

In a physical device, no gate can switch instantaneously and thus, the output of every inverter of RO changes in a finite amount of time after the input has changed. That way, it can be easily seen that adding more inverters to the chain increases the total time delay, reducing the frequency of oscillation. This way, the oscillation frequency of an RO depends on the propagation delay per stage and the number of stages used in the ring structure. Thus the frequency of oscillation is given by[6, 7]:

$$f_o = \frac{1}{2nt_d} \quad (2.2)$$

$$t_d = R_L \cdot C_{eff} \quad (2.3)$$

Where  $t_d$  is the delay per stage given by the product of the load resistance  $R_L$  and the effective output capacitance  $C_{eff}$  and  $n$  is the number of delay stages.

The oscillation frequency of an RO is thus determined from the expression of  $t_d$  which depends on the circuit parameters. The main struggle in obtaining the expression of  $t_d$  relies on the nonlinearities and parasites of the circuit.

Typically, a delay stage of a RO is built from one of the 2 different typologies:

- A. Single-ended Inverter;
- B. Differential Inverter.

### 2.2.3. Simple Inverter

A simple inverter delay cell usually comprises an NMOS and a PMOS transistor connected with a common gate as input and an additional capacitance at its output, as shown in the Fig. 2.3.

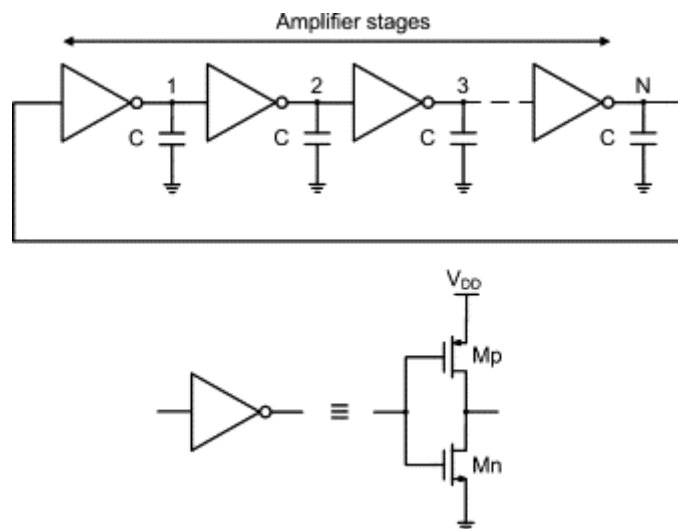


Figure 2.2- Ring Oscillator with simple inverter cells

Although this kind of approach is relatively easy to implement, and presents a small occupied area, it has also some disadvantages, namely as regards:

- i. Sensitiveness to variations in the supply voltage;
- ii. Absence of control by voltage;
- iii. Need for odd number of stages.

### 2.2.4. Differential Inverters

A  $n$  stage ring oscillator may be implemented with differential stages since they are more immune to external disturbances. If differential stages are used, the RO can have an even number of stages if the feedback lines are swapped. The topology of this structure is shown on figure 2.4.

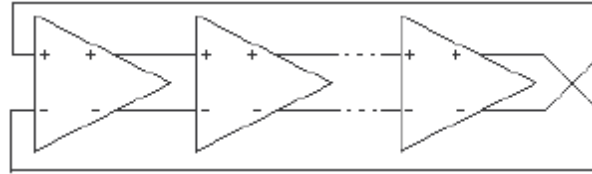


Figure 2.3- Differential Delay Ring

Although this topology presents a more complex to design when compared to a simple inverter and requires more space, it is often used due to its advantages as regards to:

- i. Noise immunity;
- ii. Less sensitiveness to variation of supply voltages;
- iii. Possibility of being implemented with an even number of stages;
- iv. It can be easily controlled by voltage.

Several topologies have been proposed for the implementation of the differential stages. In this work, the Maneatis cell will be adopted. The configuration of each cell is illustrated in the following Fig 2.5:

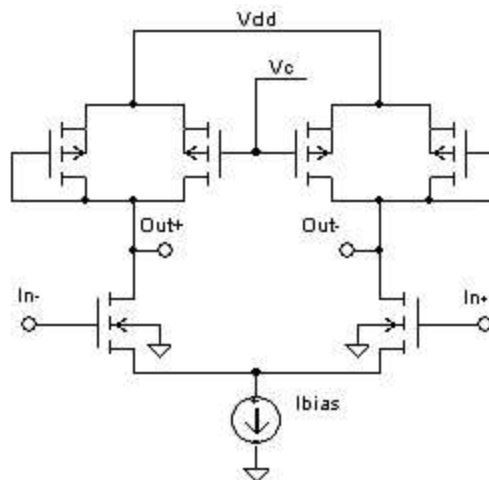


Figure 2.4- Maneatis d symmetric load delay cell [1]

In this delay cell, the current source  $I_{bias}$  is designed such that the output voltage swing is equal to the control voltage  $V_c$ .

Considering that full switching is attained in the delay cells, the frequency of oscillation is given by:

$$f_{osc} = \frac{1}{2 \cdot N \cdot t_{delay}} \quad (2.4)$$

Where  $N$  is the number of stages and  $t_{delay}$  is the delay introduced by each differential stage. For the first model proposed for ring VCOs constituted of PMOS symmetrical load, the evaluation of the delay is obtained through[9]:

$$t_{delay} = R_{eff} \cdot C_{eff} \quad (2.5)$$

Where  $R_{eff}$  represents the effective resistance of the symmetric load, and  $C_{eff}$  stands for the effective delay cell output capacitance. In order to achieve precise results, the model was used for the evaluation of the effective resistance of the symmetric load considered as the ratio between the maximum current of the load and the maximum voltage swing:

$$R_{eff} = \frac{V_{LoadMax}}{I_{LoadMax}} \quad (2.6)$$

Considering the quadratic law for the transistor drain current, the frequency of oscillation can thus be obtained by:

$$f_{osc} = \frac{\beta \cdot (V_c - V_t)}{2 \cdot N \cdot C_{eff}} \quad (2.7)$$

Yielding more accurate results for smaller values of the control voltage, a new model is proposed in[3], where it is considered the effective resistance of the symmetric load as the ratio between the maximum load voltage swing and the maximum current. Hence, the frequency of oscillation is finally given by:

$$f_{osc} = \frac{\beta \cdot (V_c - V_t)^2}{2 \cdot N \cdot C_{eff} \cdot V_c} \quad (2.8)$$

### 2.3. Ring VCO Automatic Design

Voltage Controlled Ring Oscillators are Key elements in Phase Locked-Loops (PLLs) since they are responsible for the generation of the output signal. Depending on the application of the PLL, the solution requires some design trade-offs. Typically, to achieve the desired specifications, analogue designers adopt a methodology based on iterative simulations. Although this approach provides quite accurate results, the design process is very time consuming, since the transient analyses of the circuit, essential to determine the frequency of oscillation, must run long enough until steady state is attained. Another disadvantage relies on the difficulty to achieve the desired solution given the lack of technological parameters variation information, only possible to overcome through several simulations on different conditions, making the methodology inefficient and unreliable. Therefore, the development of models based on transistor technological parameters is needed to acquire the desired robustness [1, 6, 9]. Efficient and reliable VCO models should be easy to adapt to the evolution and changing technology, taking always into account the accuracy and simplicity. Despite the fact that the accuracy of the results depends on the model, this methodology is extremely fast and the convergence to the desired solution is much easier, since there is the knowledge of the influence of each one of the parameters in the circuit behavior. This approach is thus a fundamental key for the automation of the circuit design.

In the particular case for a Ring VCO with the Maneatis cell, the frequency of oscillation is given by Eq. (2.7), which may be used for automatically design a ring oscillator. Yet, for the particular case when deep-submicron technologies are used, this model is not accurate since relies on the quadratic law for the transistor current in saturation. Considering the particular case for a seven stage ring VCO in UMC130 technology, the proposed model yields the frequency response represented in figure 2.5. The results obtained when compared to those obtained from simulating with Spectre simulator lead us to the conclusion that the proposed model, which relies on the MOSFet quadratic law, cannot be used for this technologies.

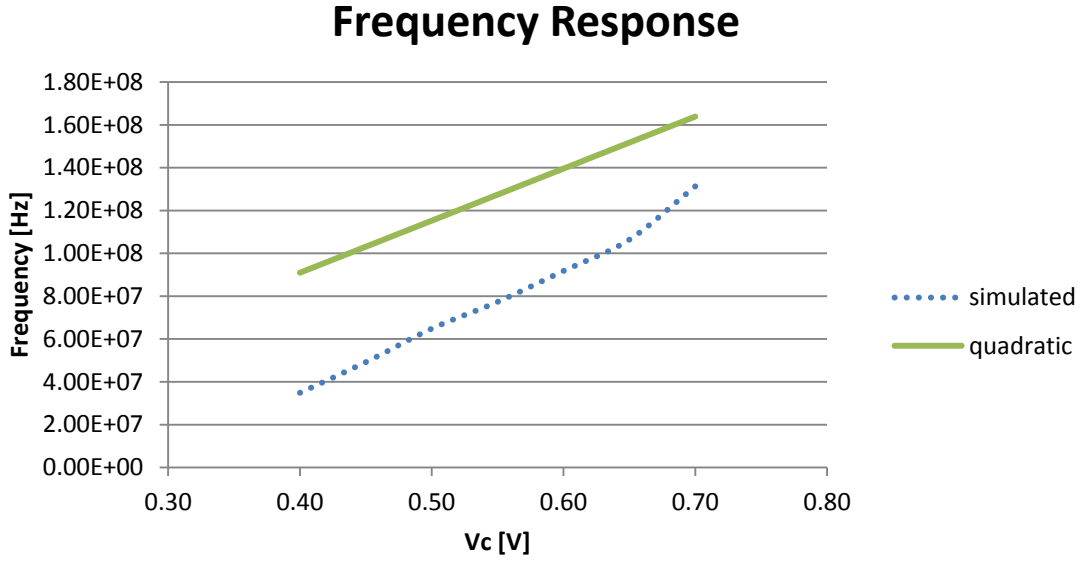


Figure 2.5 Simulated with Spectre

Thus, a new model should be used, relying on a transistor level, accurate for sub-micron technologies.

In this work, the EKV model was used in order to overcome this inaccuracy. The EKV model is a compact model which provides continuity of the large and small signal characteristics from weak to strong inversion, once a unique parameter describes the behavior in all operating regions through precise and simple equations. Also one of the strengths of this model relies on the use of one expression for modeling the drain current, capable to cover all inversion charges with a good precision for both weak and strong inversion[10-12]. Thus, the drain current is given by:

$$I_D = I_S \cdot (I_F - I_R) \quad (2.9)$$

Where  $I_F$  and  $I_R$  are the forward and reverse currents, which can be obtained through:

$$I_{F(R)} = I_S \cdot \left[ \ln \left( 1 + \exp \left[ \frac{V_P - V_{S(D)}}{2 \cdot V_t} \right] \right) \right]^2 \quad (2.10)$$

And the specific current  $I_S$  is defined as:

$$I_S = 2 \cdot \beta \cdot n \cdot V_t \quad (2.11)$$

Thus, the frequency of oscillation turns into:

$$f_{osc} = \frac{I_s \cdot (I_F - I_R)}{N \cdot V_c \cdot C_{eff}} \quad (2.12)$$

To validate the accuracy of the EKV model and compare it against the one based on the quadratic law for the transistor current, a seven stage with symmetrical differential load Ring VCO will be considered in the next subsection.

## 2.4. Working Example and Results

In order to verify the accuracy of the EKV model, a seven stage symmetrical differential load Ring VCO was considered, where each delay cell has the configuration presented in Fig. 2.5. The transistors sizes are shown in the following table.

Table 2.1- Transistor Sizes for the working example

	Load (Pmos)	Switch (Nmos)	Bias (Nmos)
W	5,0 $\mu$	40,0 $\mu$	100,0 $\mu$
L	0,5 $\mu$	0,66 $\mu$	0,5 $\mu$

This working example was considered without load capacitance. For the evaluation of the effective capacitance  $C_{eff}$ , the following approximation, explained further in this work, was used

$$C_{eff} = 0.7 \cdot C_{ox} \cdot (W_{switch} \cdot L_{switch} + W_{load} \cdot L_{load}) \quad (2.13)$$

The achieved results for this proposed VCO model are illustrated in the Fig.2.6.

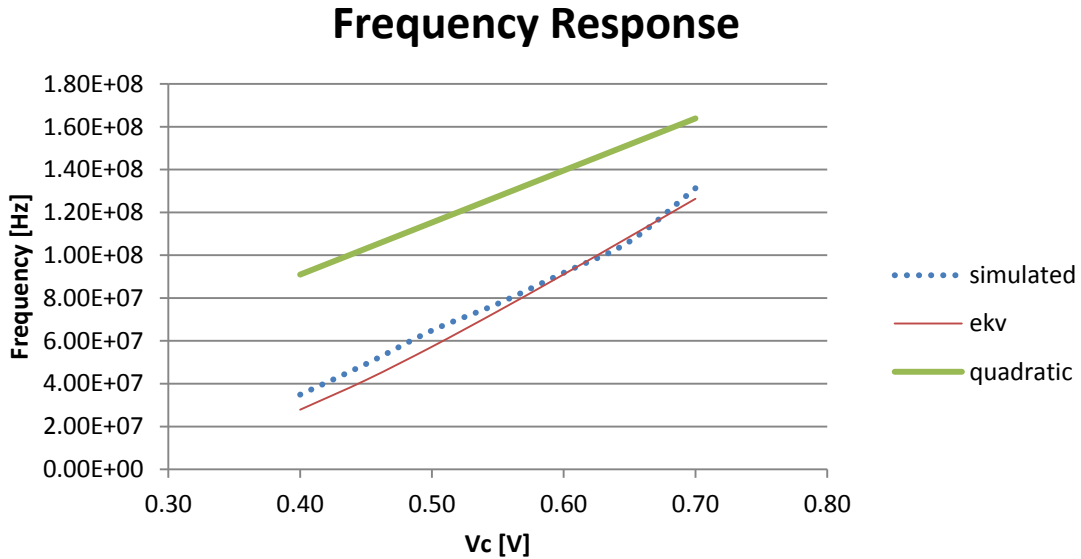


Figure 2.6- Frequency Response of the VCO



From the Fig.2.6 it is easy to conclude that when sub-micron technologies are used, the model based on the quadratic law for the transistor current presents quite inaccurate results. It is also possible to observe the accuracy of the results with the EKV model, where the majority of the points along the curve have relative errors inferior to 7%.

## 2.5. Conclusions

In this chapter a brief introduction to VCO for RF applications was given. The particular case for differential Ring VCOs with the Maneatis delay cell was presented and the corresponding models proposed in the literature were presented. The necessity for having accurate models for the automatic design of Ring VCOS was pointed out. Finally the limitations of the proposed models for VCOs in deep submicron technologies were illustrated through a working example considering a seven-stage ring oscillator. Since the inaccuracy of the results obtained with the models presented stems from the inadequacy of using the MOS quadratic model to characterize the transistors with submicron sizes, the EKV model was briefly introduced and its application for the development of the ring VCO model was proposed. Results with this new model, for the working example considered, prove the adequacy of this new model.

Further in this work, a more profound analysis on the design of a Ring VCO with symmetrical load and its limitations will be made, as well as a more profound approach to the EKV model and its parameter extraction methodology.



### 3. EKV Models

#### 3.1. Introduction

This chapter is dedicated to the use of the EKV Mosfet model for the characterization of transistors in deep-submicron technologies. After introducing the EKV model a detailed description of the methodology adopted for the determination of the EKV model parameters for the UMC130 technology is given. For the automatic determination of the EKV model parameters a script in Matlab was developed.

Finally, the validation of the model parameters obtained is accomplished through the determination of the delay introduced by single inverter stages with the EKV model. The validation is accomplished through the comparison against results obtained from simulation with Cadence Spectre.

#### 3.2. The EKV Model

The EKV Model is a charge-based physical model dedicated to the design and analysis of low-voltage and low-current circuits, built on fundamental physical properties of the MOS structure.

This compact model provides continuity of the large and small signal characteristics from weak to strong inversion, once a unique parameter set ( “This model has only 9 physical parameters, 3 fine tuning fitting coefficients, and 2 additional temperature parameters [11].”) describes the behavior in all operating regions and over all device geometries with great accuracy.

The model respects and preserves the inherent symmetry of the device by referring all the voltages, the drain voltage  $V_D$ , the source voltage  $V_S$  and the gate voltage  $V_G$ , to the local substrate (bulk), as depicted in Fig. 3.1[12]:

$$V_D = V_{DB} = |V_D - V_B| \quad (3.1)$$

$$V_S = V_{SB} = |V_S - V_B| \quad (3.2)$$

$$V_G = V_{GB} = |V_G - V_B| \quad (3.3)$$

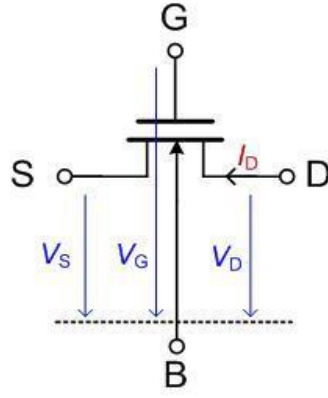


**Figure 3.1- Cross section of an idealized n-channel MOS transistor, with definitions of both voltage and current**

The transistor operating regions can be described through the surface potential  $\psi_s$  defined as the electrostatic potential at the semiconductor surface, the Fermi potential  $\varphi_F$  as the quasi-Fermi potential of the majority carriers and the channel potential  $V_{ch}$  which depends on the position along the channel and is defined as the difference between the quasi-Fermi potentials of majority and minority carriers along the channel. This channel potential represents the disequilibrium in electron distribution produced by the source and the drain voltages. The description of the different operating regions can be found in the Table 3.1[12].

**Table 3.1- Operating Regions of a EKV transistor, with respect to the surface potential**

Operating Regions	
$\psi_s < 0$	Accumulation
$\psi_s = 0$	Flat-band condition
$0 < \psi_s < \psi_F$	Depletion
$\psi_F < \psi_s < 2\psi_F + V_{ch}$	Weak inversion
$2\psi_F + V_{ch} < \psi_s < 2\psi_F + V_{ch} + mV_t$	Moderate inversion
$\psi_s > 2\psi_F + V_{ch} + mV_t$	Strong inversion

In the inversion region,  $\psi_s \gg V_t$  and thus the mobile inversion charge density  $Q'_{inv}$ , which can be defined as a function of  $V_{ch}$  and  $\psi_s$  by integrating Poisson's equation, converts to[11, 12]:

$$Q'_{inv} = -\gamma \cdot C'_{ox} \cdot \sqrt{V_t} \cdot \left[ \sqrt{\frac{\psi_s}{V_t} + \exp\left(\frac{\psi_s - 2\psi_F - V_{ch}}{V_t}\right)} - \sqrt{\frac{\psi_s}{V_t}} \right] \quad (3.4)$$

The gate voltage  $V_G$  can be obtained through the surface potential  $\psi_s$  and the mobile inversion charge density  $Q'_{inv}$  by applying:

$$V_G = V_{FB} + \psi_s + \gamma \cdot \sqrt{\psi_s} - \frac{Q'_{inv}}{C_{OX}} \quad (3.5)$$

Where  $V_{FB}$  is the flat-band voltage,  $C_{OX}$  is the gate-oxide capacitance obtained through the relation between the dielectric constant  $\epsilon_{OX}$  and the oxide thickness  $t_{OX}$ , and the body effect  $\gamma$ , which depends on the substrate doping concentration  $N_{sub}$ , given by:

$$\gamma = \frac{\sqrt{2qN_{sub}\epsilon_s}}{C_{OX}} \quad (3.6)$$

In strong inversion the surface potential  $\psi_s$  can be written as:

$$\psi_s = \psi_0 + V_{ch} \quad (3.7a)$$

Where

$$\psi_0 = 2\phi_F + mV_t \quad (3.7b)$$

Thus, expressing the inversion charge  $Q'_{inv}$  as a function of  $\psi_s$  and  $V_G$  using the Eqn. 3.5 will result:

$$Q'_{inv} = -C'_{OX} \cdot [V_G - V_{TB}(V_{ch})] \quad (3.8)$$

Where  $V_{TB}$  is the gate threshold voltage referred to the local substrate and defined as:

$$V_{TB} \equiv V_{T0} + V_{ch} + \gamma \cdot [\sqrt{\psi_0 + V_{ch}} - \sqrt{\psi_0}] \quad (3.9)$$

The threshold voltage  $V_{T0}$  is defined as the gate voltage such as  $Q'_{inv} = 0$  when the channel is at equilibrium ( $V_{ch} = 0$ ), and follows:

$$V_{T0} = V_{G|V_{ch}=0, Q'_{inv}=0} = V_{TB|V_{ch}=0} = V_{FB} + \psi_0 + \gamma \cdot \sqrt{\psi_0 + V_P} \quad (3.10)$$

The pinch-off voltage  $V_P$  is a channel potential for which, at given gate voltage, the inversion charge  $Q'_{inv}$  becomes zero, as stated in [x]. Hence

$$V_{G|V_{ch}=0, Q'_{inv}=0} = V_{TB|V_{ch}=V_P} = V_{T0} + V_P + \gamma \cdot \sqrt{\psi_0 + V_P} - \sqrt{\psi_0} \quad (3.11)$$

The latter equation can be expressed in terms of the gate voltage by simply inverting Eqn. 3.11:

$$V_P = V_G - V_{T0} - \gamma \cdot \left[ \sqrt{V_G - V_{T0} + \left( \sqrt{\psi_0} + \frac{\gamma}{2} \right)^2} - \left( \sqrt{\psi_0} - \frac{\gamma}{2} \right) \right] \quad (3.12)$$

The value of  $V_{T0}$  can also be determined by the value of  $V_G$  corresponding to the point where the pinch-off voltage  $V_P$  is zero ( $V_{T0} = V_G$  when  $V_P = 0$ ). The derivative of the gate voltage with respect to the pinch-off voltage is defines as the *slope factor*  $n$  and is given by:

$$n \equiv \frac{dV_G}{dV_P} = 1 + \frac{\gamma}{2 \cdot \sqrt{\psi_0 + V_P}} \quad (3.13)$$

The pinch-off voltage and the slope factor as functions of the gate voltage are depicted in Fig.3.2:

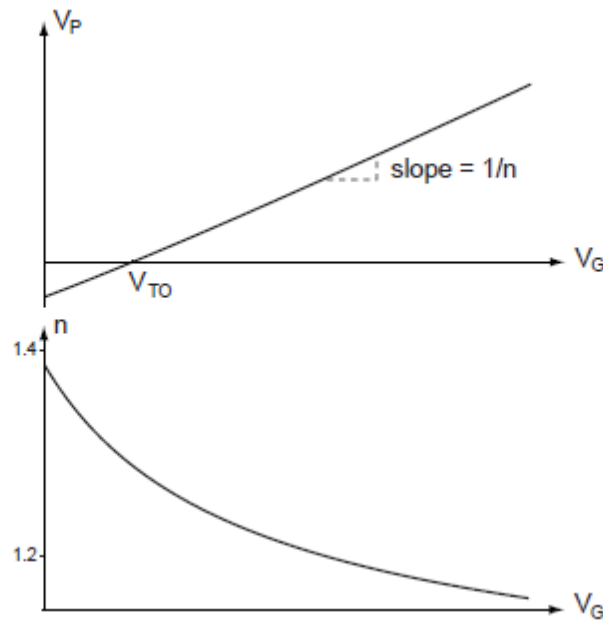


Figure 3.2- Pinch-off voltage and slope factor as function of the gate voltage

By applying the definition of the pinch-off voltage into Eqn. 3.8, the inversion charge  $Q'_{inv}$  results:

$$Q'_{inv} = -C'_{ox} \cdot [V_P - V_{ch} + \gamma \cdot (\sqrt{\psi_0 + V_P}) - \sqrt{\psi_0 + V_{ch}}] \quad (3.14)$$

It is possible to deduce that the pinch-off voltage can be interpreted as the equivalent effect of the gate voltage referred to the channel.

### 3.2.1. Weak inversion

The inversion charge decreases smoothly down to zero as the channel leaves strong inversion. When the channel voltage  $V_{ch}$  becomes smaller than the pinch-off voltage  $V_p$ , the channel is in weak inversion and the inversion charge becomes negligible with respect to the depletion charge. Hence, introducing the definition of  $V_{T0}$ , the gate voltage becomes[11, 12]:

$$V_G = V_{T0} + (\psi_s - \psi_0) + \gamma \cdot (\sqrt{\psi_s} - \sqrt{\psi_0}) \quad (3.15)$$

Although  $V_p$  has been defined in strong inversion operation, it can also be used in weak inversion to approximate the surface potential. Comparing the Eqn. 3.15 and Eqn. 3.11, the surface potential can be obtained by applying:

$$\psi_s = \psi_0 + V_p \quad (3.16)$$

By introducing the result in the solution of the Poisson equation in (3.4) and applying the Taylor expansion, the inversion charge in weak inversion can be approximated to a simplified expression:

$$Q'_{inv} = -C'_{ox} \cdot (n - 1) \cdot V_t \cdot \exp\left(\frac{\psi_0 - 2 \cdot \psi_F}{V_t}\right) \cdot \exp\left(\frac{V_p - V_{ch}}{V_t}\right) \quad (3.16)$$

### 3.2.2. Drain Current

The drain current is obtained by integrating the inversion charge along the channel, from the source ( $V_{ch} = V_S$ ) to the drain ( $V_{ch} = V_D$ ), assuming constant mobility along the channel:

$$I_D = \beta \cdot \int_{V_S}^{V_D} -\frac{Q'_{inv}}{C_{ox}} dV_{ch} \quad (3.17)$$

Where:

$$\beta = \mu_0 \cdot C'_{ox} \cdot \frac{W_{eff}}{L_{eff}} \quad (3.18)$$

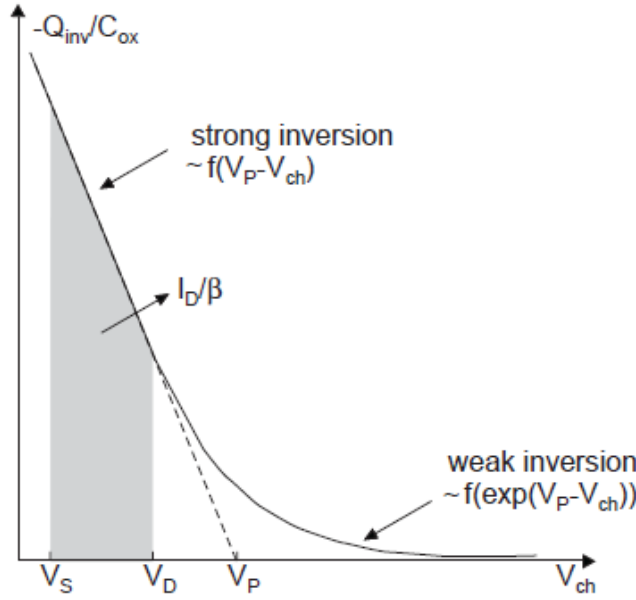


Figure 3.3- Inversion charge as a function of the channel potential

The inversion charge as a function of the channel potential is illustrated in Fig. 3.3. Since the drain current is determined by integration of the inversion charge along the channel potential, it is proportional to the shaded surface comprised between the source and the drain voltage. The integral can be rewritten by decomposing into a forward current  $I_F$  and a reverse current  $I_R$  defined by[10-12]:

$$I_D = \beta \cdot \int_{V_S}^{\infty} -\frac{Q'_{inv}}{C_{ox}} dV_{ch} - \beta \cdot \int_{V_D}^{\infty} -\frac{Q'_{inv}}{C_{ox}} dV_{ch} = I_F - I_R \quad (3.19)$$

The forward current corresponds to area delimited by the difference  $V_P - V_S$ , while the reverse current corresponds to the area delimited by the difference  $V_P - V_D$ . It is possible to conclude that when the drain voltage  $V_D$  is increased, the area corresponding to the difference  $V_P - V_D$  is reduced and therefore the reverse current is reduced. The forward saturation is attained when the drain voltage reaches the pinch-off voltage  $V_P$ , which will make the channel to pinched-off at the drain and the reverse current becomes zero ( $I_R = 0$ ). Thus, in forward saturation the drain current becomes equal to the forward component of the current  $I_F$ . Another conclusion possible to extract from the figure, is the fact that the inversion charge  $Q'_{inv}$  is an exponential function of  $V_P - V_{ch}$ , in weak inversion, which results in an exponential forward(reverse) current  $I_F(I_R)$ :

$$I_{F(R)} = I_S \cdot \exp \left[ \frac{V_P - V_{S(D)}}{V_t} \right] \quad (3.20)$$



Where  $I_s$  is defined as the specific current given by:

$$I_s = 2 \cdot \beta \cdot n \cdot V_t \quad (3.21)$$

The specific current characterizes the drain current when the transistor operates in the center of moderate inversion, and depends on technology and transistor geometry. Thus the specific current plays an important role as design parameter that helps sizing the transistor to an imposed bias current and a given mode of operation.

Making use of the approximations for the inversion charge presented above in this chapter, it is possible to obtain the expressions for the forward and reverse currents for both weak and strong inversion. Since, it is important to determine one expression capable to cover all inversion charges with a good precision, mathematical interpolation is applied yielding, the expression valid for all the different inversions is given by:

$$I_{F(R)} = I_s \cdot \left[ \ln \left( 1 + \exp \left[ \frac{V_P - V_{S(D)}}{2 \cdot V_t} \right] \right) \right]^2 \quad (3.22)$$

Finally, the drain current is given by:

$$I_D = I_s \cdot (I_F - I_R) \quad (3.23)$$

The parameter extraction methodology along with the model validation will be presented in the next subsection.

### 3.3. Parameters Extraction

This section describes the parameter extraction methodology, as well as the results obtained and their validation.

#### 3.3.1. Drain Current

As already mentioned in the presentation of the EKV model, the drain current is decomposed in a forward and reverse current  $I_F$  and  $I_R$ , combined in a single expression for linear and saturation regimes and valid from weak to strong inversion. These currents are functions of  $V_P - V_D$  and  $V_P - V_S$  respectively:

$$I_D = I_F(V_P - V_D) - I_R(V_P - V_S) \quad (3.24)$$

The expression for the drain current can be obtained applying a normalization factor called specific current  $I_S$ :

$$I_{F(R)} = I_S \left[ \ln \left( 1 + \exp \left[ \frac{V_P - V_{S(D)}}{2 \cdot U_T} \right] \right) \right]^2 \quad (3.25)$$

Where  $I_S$  is obtained through a parameter extraction and  $U_T \equiv k \cdot T/q$ .

#### 3.3.2. Extraction of $I_{specific}$

In the MOS transistor saturation region, the reverse current  $I_R$  approaches zero and so becomes negligible with respect to forward current  $I_F$ . Therefore, the drain to source current can be approximated by[13]:

$$I_{ds} = I_{specific} \cdot I_f = I_{specific} \cdot \left[ \ln \left( 1 + \exp \left[ \frac{V_P - V_S}{2 \cdot U_T} \right] \right) \right]^2 \quad (3.26)$$

In saturation  $\exp \left[ \frac{V_P - V_S}{2 \cdot U_T} \right] \gg 1$ , yielding

$$I_D = I_F(V_P - V_D) - I_R(V_P - V_S) \quad (3.27)$$

Hence

$$\frac{\partial(\sqrt{I_{ds}})}{\partial V_s} = -\sqrt{\frac{I_{specific}}{(2 \cdot U_T)^2}} = -slope \quad (3.28)$$

And thus

$$I_{specific} = 4 \cdot slope^2 \cdot U_T^2 \quad (3.29)$$

Given (3.28), the  $I_{specific}$  can be extracted by applying a fixed gate voltage and determine the strong inversion slope of the  $\sqrt{I_D}$  vs  $V_s$  characteristic[13, 14]. To find the value of the slope, a fitting of the characteristic obtained in simulation with a straight line was applied, using the optimization tool available in Matlab.

A configuration of the circuit used to measure the  $I_{specific}$ , as well as the simulation result, are illustrated in the figure 3.4a and 3.4b respectively.

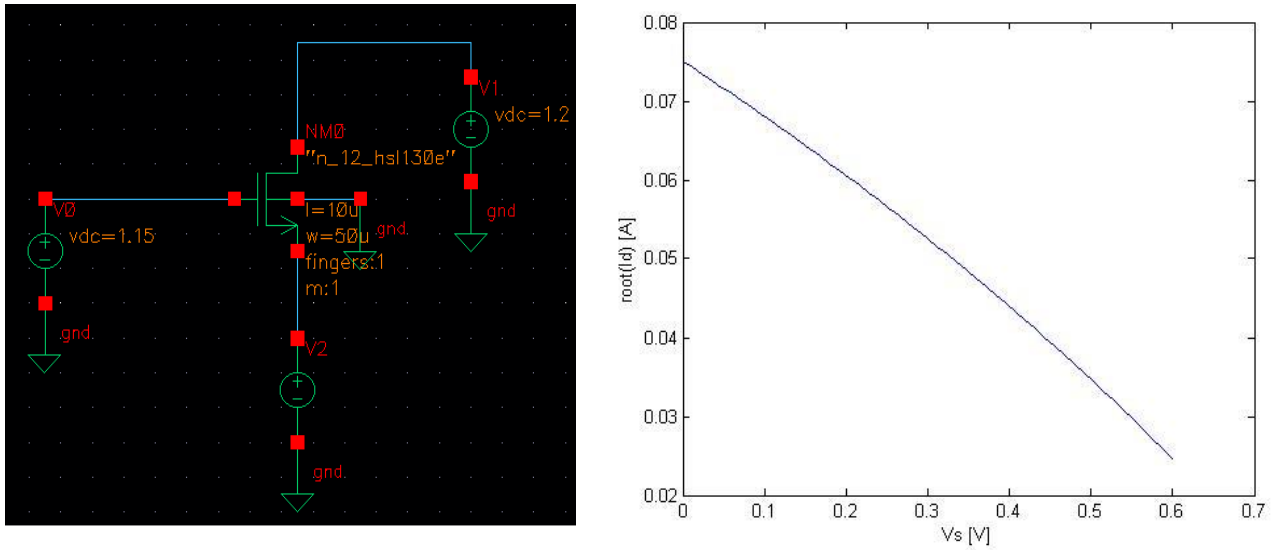


Figure 3.4- A - Circuit configuration for specific current extraction. W=50u, L=10u ; B - Root (Id) vs Vs characteristic

### 3.3.3. The Pinch-off Voltage

The pinch-off voltage  $V_P$  corresponds to the value of the channel potential for which the inversion charge density extrapolated from strong inversion becomes zero[13, 14].

$$V_P = V'_G - \varphi - \gamma' \cdot \left[ \sqrt{V'_G + \left(\frac{\gamma'}{2}\right)^2} - \frac{\gamma'}{2} \right] \quad (3.30)$$

$$V'_G = V_G - V_{TO} + \varphi + \gamma \cdot \sqrt{\varphi} \quad (3.31)$$

Where  $V_{TO}$  is the threshold voltage defined as the gate voltage for which the inversion charge forming the channel is zero at the equilibrium ( $V_P = 0$ ),  $\varphi$  is the approximation of the surface potential in strong inversion and  $\gamma$  is the body effect and given by

$$\gamma = \sqrt{2q\epsilon_{si}N_{sub}}/C_{ox} \quad (3.32)$$

These parameters can be extracted through a fitting of the  $V_P$  vs  $V_G$  characteristic, using the circuit configuration presented in Fig. 3.5a. Note that, in this configuration, the value of the current source must be half of the specific current. The characteristic obtained in the simulation is illustrated in Fig.3.5b.

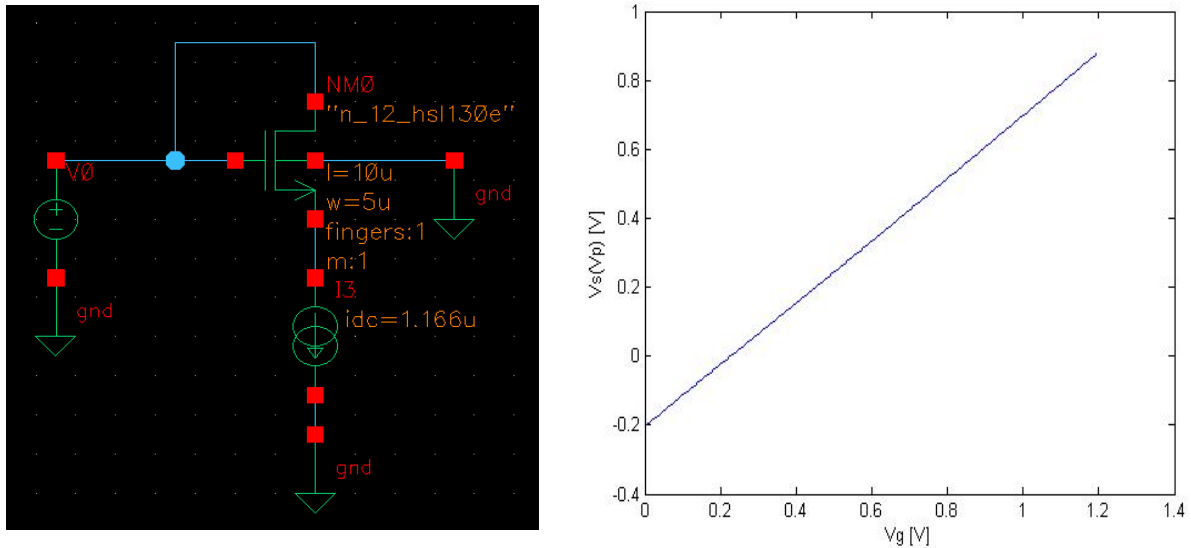


Figure 3.5- A- Circuit for measuring the  $V_P$  vs  $V_G$  characteristic ; B-  $V_P$  vs  $V_G$  characteristic

Through this measures it's also possible to obtain the weak inversion slope factor  $n$ , defined as the inverse of the partial derivative of the pinch-off voltage with respect to the gate voltage, and so:

$$n \equiv \left[ \frac{\partial V_P}{\partial V_G} \right]^{-1} = \left( 1 - \frac{\gamma}{2 \cdot \sqrt{V_P + \varphi}} \right)^{-1} \quad (3.33)$$

Once found the slope factor  $n$ , the value for the parameter  $\beta$  can be obtained through:

$$\beta = K_p \cdot \frac{W}{L} \cdot \frac{1}{1 + \theta \cdot V_P} \quad (3.34)$$

Although, it is needed to acquire the mobility reduction coefficient  $\theta$ . This parameter can be achieved through a fitting of the  $V_G$  versus  $I_D$  characteristic using the same circuit configuration, since:

$$I_{specific} = 2 \cdot n \cdot \beta \cdot U_T^2 \quad (3.35)$$

In saturation,

$$I_D = \frac{I_s}{4 \cdot U_T^2} \cdot (V_P - V_S)^2 \quad (3.36)$$

Thus,

$$I_D = \frac{n}{2} \cdot V_P^2 \cdot \beta = \frac{n}{2} \cdot V_P^2 \cdot K_p \cdot \frac{W}{L} \cdot \frac{1}{1 + \theta \cdot V_P} \quad (3.37)$$

Also notice that the approximation  $\gamma' = \gamma$  it is just valid for large devices, otherwise the correct body effect  $\gamma'$  fact has to be taken into account.

This way  $V_P$  depends on the effective channel length and width, as well as on the drain and source voltages  $V_D$  and  $V_S$ , due to coefficients  $LETA$  for short-channel and  $WETA$  for small-channel effects, through the following expression[14]:

$$\gamma' = \gamma - \frac{\varepsilon_s}{C_{ox}} \cdot \left[ \frac{LETA}{L + DL} \cdot \sqrt{\varphi + V_D} + \left( \frac{LETA}{L + DL} - \frac{3 \cdot WETA}{W + DW} \right) \cdot \sqrt{\varphi + V_S} \right] \quad (3.38)$$

The pinch-off voltage extraction consists in using a constant current bias, typically equal to half of the specific current  $I_S$  as mentioned before, to measure the  $V_P$  versus  $V_G$  characteristic in moderate inversion by sweeping the gate voltage and measuring the source voltage  $V_S \approx V_P$ .

As it was said above,  $V_{TO}$  is determined by a certain value of  $V_G$  corresponding to the point where  $V_P$  crosses zero ( $V_{TO} = V_G$  when  $V_P = 0$ ), being the unique parameter without need of extrapolation. The parameters  $\varphi$  and  $\gamma$  are extracted by fitting (3.30) to the measured characteristic. In the figure 3.6 can be found the results of this extraction as well as its correctness, where the straight line is the characteristic measured and the symbol plus is the characteristic achieved by applying the values of the parameters.

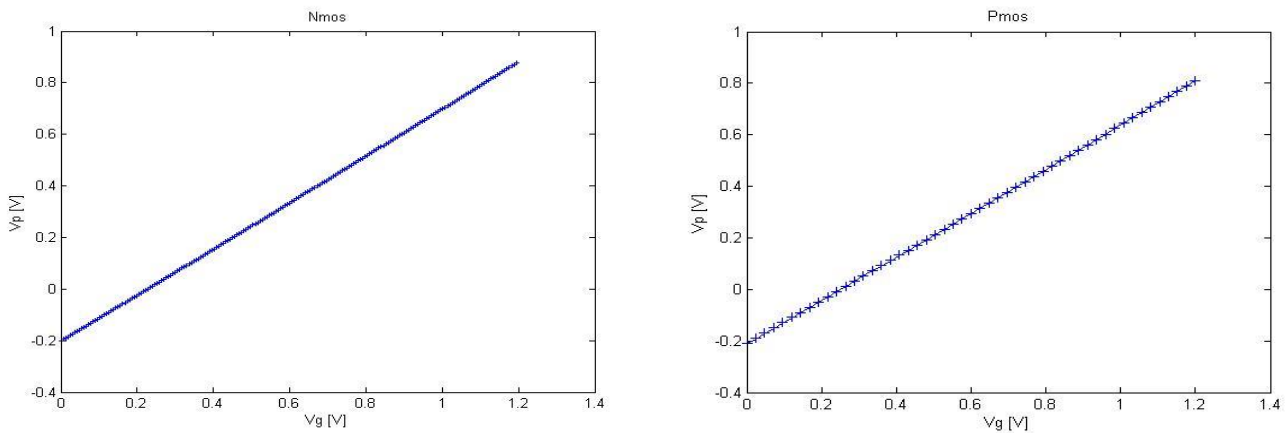


Figure 3.6- Estimated vs Simulated results from  $V_p$  vs  $V_g$  characteristic. Nmos:  $W=50\mu$ ,  $L=10\mu$ . Pmos:  $W=10\mu$ ,  $L=1\mu$

Once these parameters for large devices are obtained, the parameters  $LETA$  and  $WETA$  can be extracted from the measured pinch-off voltage characteristic (short-channel and narrow-channel respectively) by fitting (3.38) but taking into account the correct body effect. Note that in the extraction of  $LETA$ , thus for a device with a short-channel length, the coefficient  $WETA$  is neglected, and vice-versa. This way, the accuracy of the results for this extraction is founded on the figure 3.7, where it is possible to observe the characteristic measured as well as the characteristic achieved using the obtained values for the transistor PMOS.

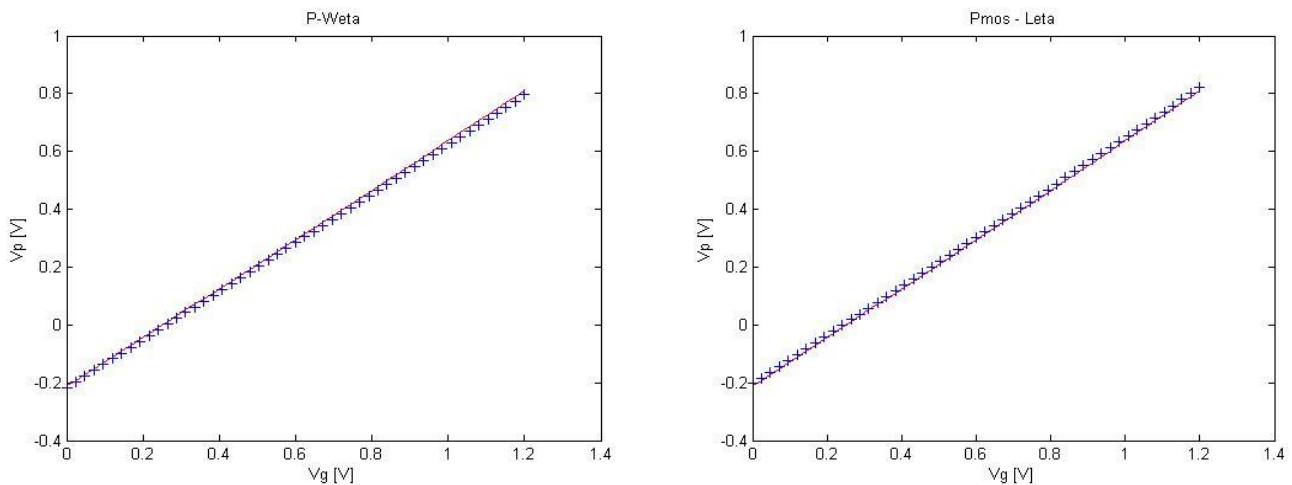


Figure 3.7- WETA and LETA Pmos extraction from  $V_p$  vs  $V_g$  characteristic

Finally, the parameters values obtained for both NMOS and PMOS transistors are presented in the following tables.

**Table 3.2 Nmos transistor Parameters**

NMOS							
$I_{specific}$ (uA)	$V_{TO}$ (V)	$\Gamma$	$\Phi$	$\beta$	$W_{eta}$	$L_{eta}$	$\theta$
2,33	0,1875	0,209	0,7234	0,002	0,344	0,0351	0,9765

**Table 3.3 Pmos transistor Parameters**

PMOS							
$I_{specific}$ (uA)	$V_{TO}$ (V)	$\Gamma$	$\Phi$	$\beta$	$W_{eta}$	$L_{eta}$	$\theta$
1,63	0,2508	0,4594	1,4088	9,65E-4	0,0869	0,0083	0,25

In order to check the accuracy of the parameters extracted, the  $I_D(V_{gs})$  characteristic obtained with the EKV model was compared against simulation results as presented in the Fig. 3.8.

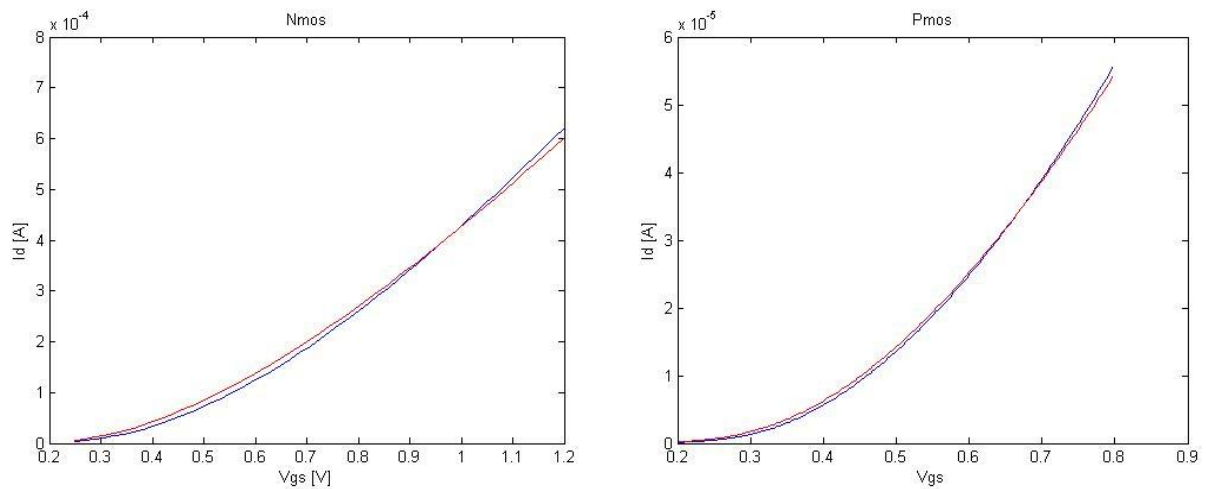


**Figure 3.8 Estimated (red) vs Simulated (blue) current of an Nmos and Pmos respectively**

From the Fig. 3.8, it is possible to consider that the results are quite acceptable and thus the values for the parameters valid.

For validating the results obtained in all regions of operation of the MOS transistor, the transient response of a CMOS inverter will be considered in the next subsection.

### 3.3.4. Automatic Generation of the EKV Model Parameters

For the automatic generation of the EKV model parameters a script was developed in Matlab. The source code for this script can be found in Annex I.

The script developed starts by considering the DC simulation response from the circuit represented in figure 3.4. From these results, the square root of the drain current values for each source voltage is evaluated and the value for the specific current  $I_s$  is obtained.

Once obtained the specific current  $I_s$ , the script considers the DC simulation of the circuit with the configuration presented in figure 3.5. From these results, the values of  $V_s$  and  $V_g$  are considered in an optimization tool provided by Matlab, to fit the data obtained to the expression for the pinch-of-voltage represented by the equation (3.30), and the values for the parameters  $\varphi$  and  $\gamma$  are obtained. Through the estimation of the values of the pinch-of-voltage, the weak inversion slope factor  $n$  using the equation (3.33) it is obtained.

For the evaluation of the parameter  $WETA$ , the script considers the DC simulation of the circuit with the same configuration as in figure 3.5, although with a smaller value for the width of the transistor. From the results obtained, the pinch-of-voltage is evaluated in order to obtain the values for the correct body effect  $\gamma'$  through the equation (3.30). The next step, where the parameter  $WETA$  is obtained, is to introduce again in the optimization tool the results obtained from the evaluation of the correct body effect  $\gamma'$  to fit into the expression (3.38) considering  $LETA = 0$ . The inverse procedure is considered for the evaluation of the parameter  $LETA$ .

Finally, the script considers again the DC simulation response from the circuit represented in figure 3.5. From these results, the values of the drain current are introduced in the optimization tool for a fitting to the equation (3.7) and the value for the parameter related to the mobility reduction coefficient  $\theta$  is obtained. After the evaluation of the parameter  $\theta$ , the parameter  $\beta$  is obtained through the expression (3.34).



## 3.4. Work Examples

### 3.4.1. Single Inverter

Extracted all the EKV model parameters needed for the study and carried out its verification and validation, a Matlab prototype was built, with functions based on the model equations, in order efficiently study the behavior of the transistor for different circuits topologies. With the interest of verifying the model accuracy, a comparison was made on the behavior of an inverter in a Cadence simulation against the behavior obtained through the model designed.

The results obtained were quite satisfactory, since the output curves of the model match with the output curves obtained through simulation as it is possible to observe in figure 3.9, where the straight line corresponds to the output estimated and the symbol plus correspond to the output simulated.

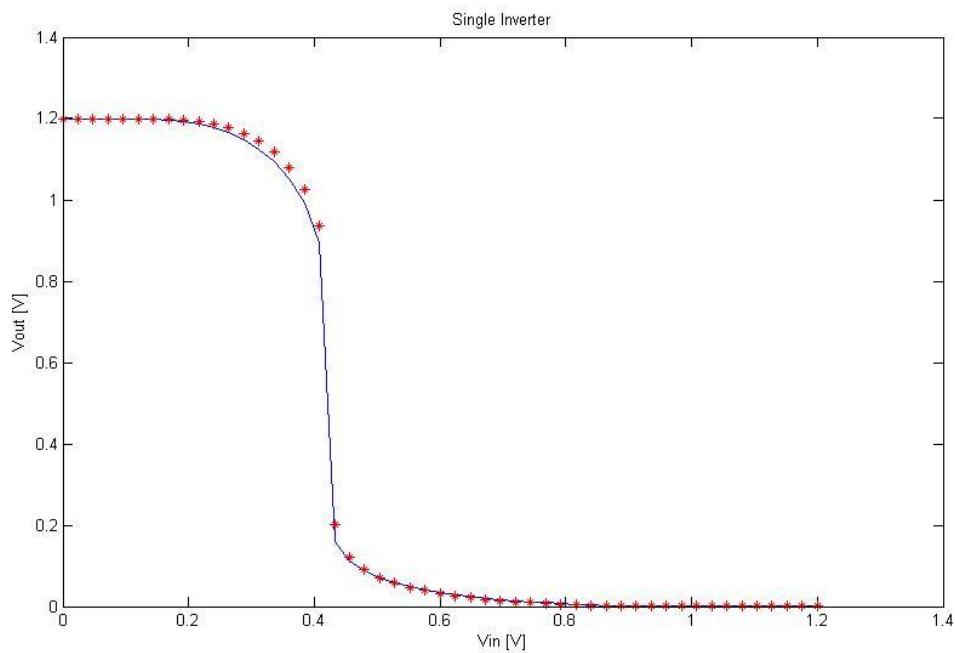


Figure 3.9- Estimated vs Simulated output for one stage inverter. Nmos: W=20u, L=5u. Pmos: W=80u, L=20u

### 3.4.2. Three Stages Inverter

In a second example, the circuit with three inverters represented in Fig. 3.9 was considered. This topology was adopted in order to check the delay between stages.

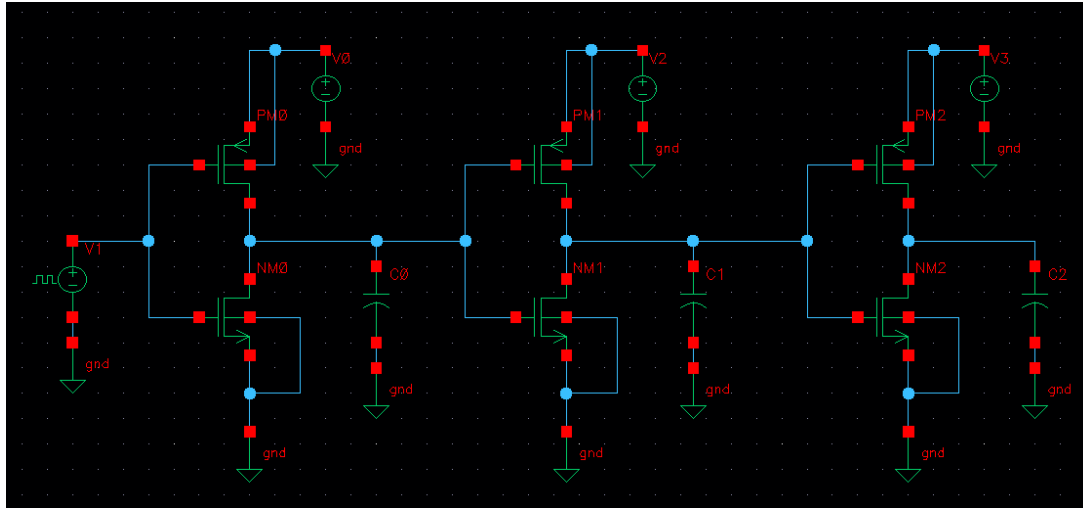


Figure 3.10- Three Stage Inverter Configuration. Nmos:  $W=20\mu$ ,  $L=5\mu$ . Pmos:  $W=80\mu$ ,  $L=10\mu$

From the Fig. 3.10 below, it is possible to conclude that the model designed presents the expected behavior. The output obtained from the model is an excellent approximation to the one obtained from the simulation.

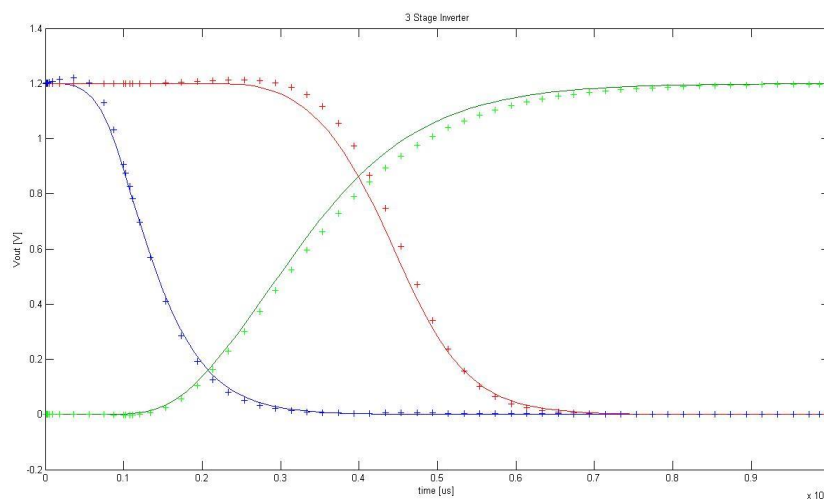


Figure 3.11- Estimated vs Simulated output for a three stage inverter

The values of the delays between stages as well as the respective relative errors are presented in the following Table 3.4.

**Table 3.4 Model vs Simulation delays and relative error**

Delay Matlab		Delay Cadence		Relative Error [%]
Stage 1 to 2	1,91E-07	Stage 1 to 2	2,04E-07	-6,53
Stage 1 to 3	3,13E-07	Stage 1 to 3	3,24E-07	-3,42
Stage 2 to 3	1,22E-07	Stage 2 to 3	1,20E-07	1,87

The relative errors may be due to the fact that the model does not consider yet the parasite capacitances of each transistor. However the results were quite accurate since the highest relative error is inferior to 7%.

From the results obtained with the working examples described above, it is possible to conclude that the parameters extracted present a good accuracy making the model valid.

### 3.5. Conclusions

In this chapter an introduction to EKV Mosfet model was given. The methodology adopted for the evaluation of the EKV model parameters was carefully described. A Matlab script for evaluating the EKV model parameters for both NMOs and PMOs transistors was developed and the results obtained for UMC130 technology transistors were presented. The validity of the parameters obtained was carried out through comparison with simulation results with Cadence, for the determination of  $I_D(v_{gs})$  characteristics of both NMOs and PMOs transistors. Finally working examples considering the generation of the output characteristic of a switching inverter and the determination of delays for a chain of inverters were considered. The accuracy of results, checked against simulation with Cadence Spectre is demonstrated.

These results lead us to the conclusion that the EKV model is adequate for the characterization of symmetrical-load ring VCOs. In the next chapter, the application of the EKV model for the characterization of Ring-VCOs and further application to the optimization-based design of VCOs is addressed.



## **4. Project of a VCO with EKV Model**

### **4.1. Introduction**

This Chapter addresses the optimization-based design of Nmos symmetric load ring VCOs. After a brief introduction to optimization-based design methodologies, the new model for characterizing the NMOs symmetric Load Ring VCO in submicron technologies will be presented. The validity of the VCO model for UMC130 Technology will be checked against simulation results. Finally, working examples considering the optimization based design of ring VCOs for oscillation frequencies up to 1.7 GHz will be presented.

### **4.2. Ring VCO Design Considerations**

The design of analog blocks is usually performed through an iterative process. Designers start with a first solution based on very simple models and then, using heuristic rules altogether with electrical simulation, in an iterative procedure, perform the tuning of the design solution fitting to the envisaged specifications. During the last years, the necessity for designing analog/RF building blocks with ever more stringent specifications that push the circuits to the limits of the feasibility allowed by the technologies makes the use of optimization methodologies more popular[1, 6, 9].

Regarding optimization two different approaches may be considered. In a first methodology, that mimics the analog design previously described, the electrical simulator is integrated into an optimization engine. Sometimes, dedicated tools are developed which also allow the inclusion of heuristics into the optimization loop. In the particular case for ring VCOs this electrical simulation based optimization approach is not an efficient solution, since the characterization of VCOs is accomplished through lengthy transient simulations. In this case, the optimization should be performed using an accurate and not very complex VCO model.

In chapter 2 a simple and accurate model for evaluating the oscillation frequency of an NMOs symmetric load ring VCO was proposed. The accuracy of the model, when applied to submicron technologies is granted through the use of the EKV transistor model.

Yet for introducing this model into an optimization loop it is fundamental to understand the validity limits of the model, so that feasible design solutions are obtained. If we use the model

validity limits, we will be restricting the design space and a more efficient optimization is attained.

Furthermore, an evaluation of the design trade-offs will help understand the key factors in the design process.

In the next subsections some considerations regarding the qualitative influence of the several elements comprising the Maneatis cell, as illustrated in Fig. 4.1, will be studied.

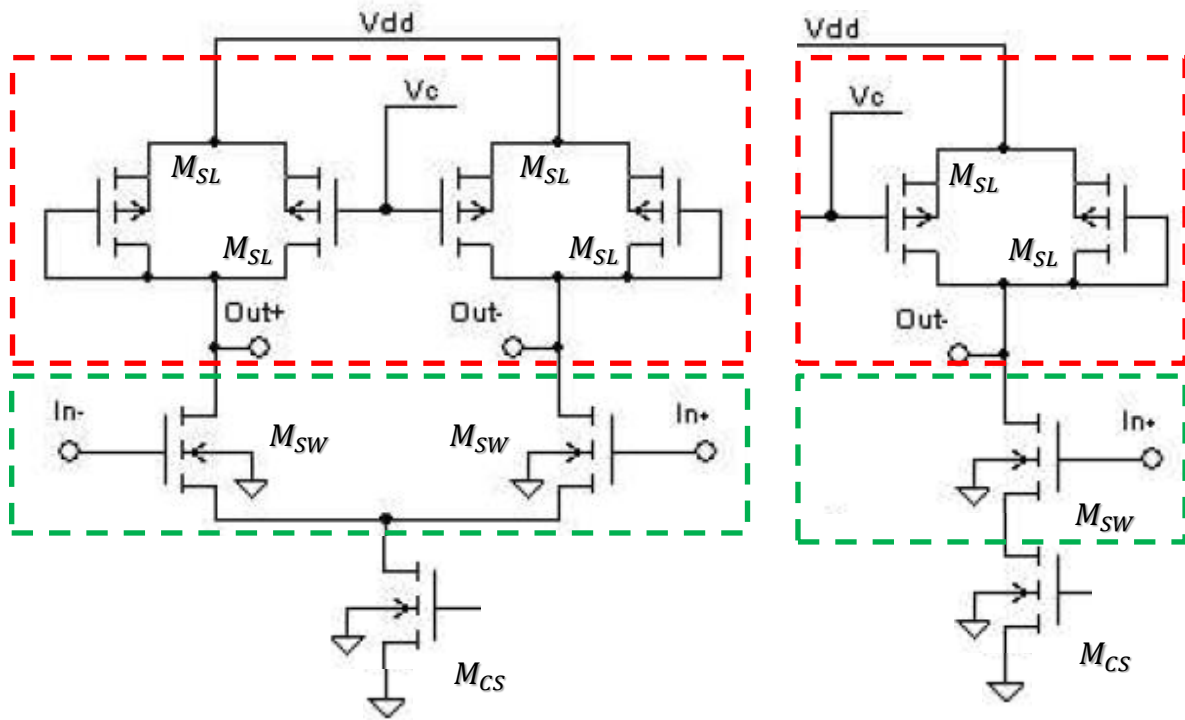


Figure 4.1- Maneatis cell and Bias Current Source

In the Fig. 4.1 is presented the configuration of the Maneatis cell, where the red section corresponds to the symmetric load cell while the green section represents the transistors responsible for the switching, as well as the bias current source. The current source used grants an oscillator output signal swing equal to the control voltage  $V_c$ . For the model to be valid, we must guarantee that the biasing current source remains in the saturation region, and that the switching transistors  $M_{SW}$  may be approximated to ideal switches. These considerations raise a limit to the maximum value of  $V_c$  that prevents both the biasing and the switching transistors to enter triode region of operation.

Through the inspection of the proposed model, Eq. (2.12) we may conclude that the frequency of oscillation depends, fundamentally on the current provided by the bias stage and on the load capacitance.

In the next subsection the influence of each of these elements will be studied.

#### 4.2.1. Bias Stage

A first analysis on the influence of the bias transistors size is evaluated. As it was already said, the current source  $I_{bias}$  of the Maneatis cell is designed such that the output voltage swing is equal to the control voltage  $V_C$ . In order to understand its influence, a simulation was made for different sizes of the bias transistors, for an oscillator with seven stages.

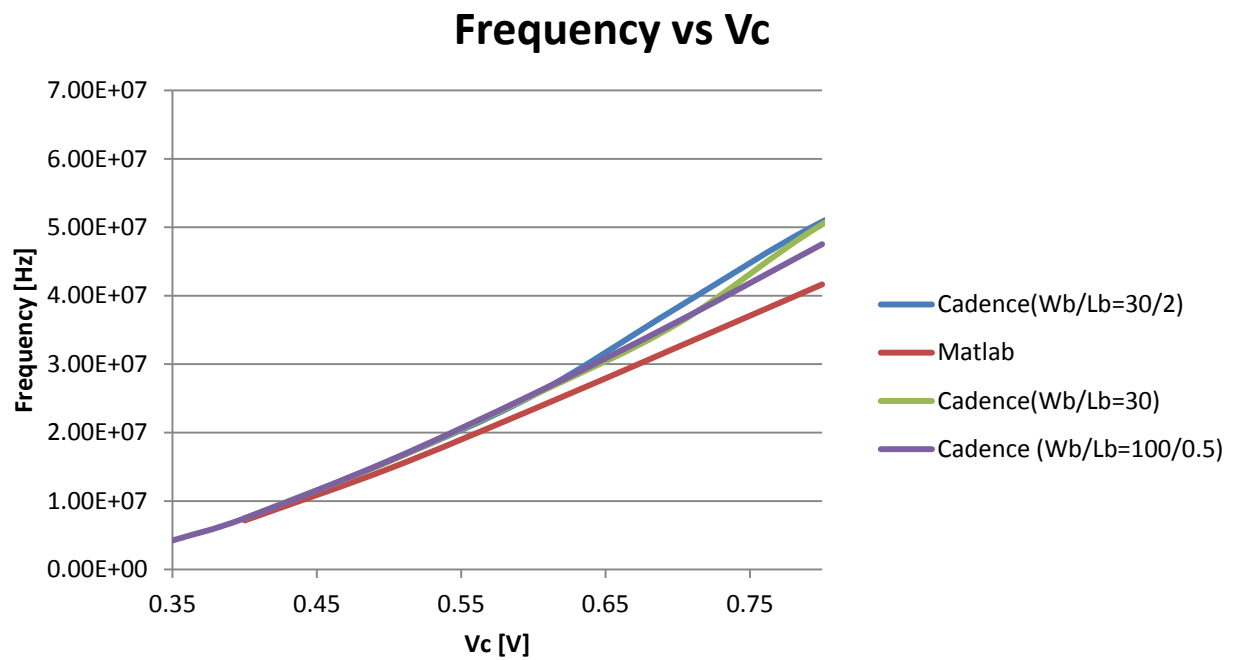


Figure 4.2- Frequency vs Vc characteristic of the 7 stages R-VCO for different sizes of the bias transistors

In the Fig.4.2 above is presented the **Frequency** vs **V<sub>c</sub>** characteristic of the ring oscillator with 7 stages obtained through the Cadence simulations against the characteristic estimated through the Matlab simulation. Since the model implemented in Matlab does not take into account the bias transistor sizes, only one response is obtained. There are several conclusions possible to extract from this chart.

The first point relies on the difference between the frequency values of the Cadence simulations against the one from Matlab. In this case a load capacitance of 2F was used as a way of using an approximate model that does not take into account the mosfet capacitances. This approximation may justify the difference between the simulated and the results obtained with the matlab model.

Another analysis possible to extract, relies on the influence of the W/L ratio of the bias stage transistors. It is possible to observe that for higher values of W/L, the curve approximates to a linear function (for a control voltage not exceeding the boundaries of  $0.4 < V_c < 0.8$ , otherwise the bias stage will not work properly), and to values similar from the ones estimated in Matlab. The latter happens due to the increase of the current with the W/L ratio, which will make the bias transistor maintain the saturation for lower values of  $V_{ds}$ .

In the next sub-section, an analysis on the approach used to calculate the effective capacitance of the oscillator will be presented since it will have a direct influence on the output frequency and thus on the design of the switch and load transistors.

#### 4.2.2. Effective Capacitance

With the purpose of taking into consideration, in the model designed in Matlab, the parasitic capacitances of the transistor, a study was carried out in order to check the accuracy of the results using the following approximation for the effective capacitance[6]:

$$C_{eff} = K \cdot C_{ox} \cdot (W_{switch} \cdot L_{switch} + W_{Load} \cdot L_{Load}) \quad (4.1)$$

For the development of this study, several simulations were made with the oscillator composed by 3, 5 and 7 stages without load capacitance and changing the size of the switch and the load transistors. The value of the effective capacitance of the oscillator was obtained through the expression of the frequency of oscillation given by:



$$frequency = \frac{I_{sl}}{N \cdot V_c \cdot C_{eff}} \quad (4.2)$$

And thus,

$$C_{eff} = \frac{I_{sl}}{N \cdot V_c \cdot f} \quad (4.3)$$

Once obtained the results of the different simulations, a comparison was made between the values of the effective capacitance of the simulation and the ones estimated by the model, presented in the Table 4.1 below. Notice that the values presented were obtained for a 7 stages oscillator, using a control voltage of 0.6V for the simulations and  $K = 0.66$  for the estimation of the equivalent capacitance in the model.

**Table 4.1- Capacitance simulated vs Capacitance estimated**

$W_{load}$	$L_{load}$	$W_{sw}$	$L_{sw}$	$C_{simulated}[pF]$	$C_{estimated}[pF]$	<b>Relative Error [%]</b>
21,3μ	0,5μ	10μ	0,33μ	0,211	0,198	6,94
42,6μ	0,5μ	10μ	0,33μ	0,106	0,112	-6,18
42,6μ	0,5μ	20μ	0,66μ	0,283	0,28	1,29
42,6μ	0,5μ	30μ	0,66μ	0,309	0,335	-7,61
42,6μ	0,5μ	40μ	0,66μ	0,341	0,39	-12,58

It is also important to observe the influence of this approach in the values estimated for the frequency of oscillation when compared to the values of the simulation. This way, a comparison is made between the frequency values of the simulation and the estimated ones, for the same size of the transistors, as presented in the following table 4.2.

**Table 4.2 Frequency simulated vs Frequency estimated**

$W_{load}$	$L_{load}$	$W_{sw}$	$L_{sw}$	$Freq_{simulated}[GHz]$	$Freq_{estimated}[GHz]$	<b>Relative Error [%]</b>
21,3μ	0,5μ	10μ	0,33μ	0,451	0,504	-10,53
42,6μ	0,5μ	10μ	0,33μ	0,451	0,442	2,20
42,6μ	0,5μ	20μ	0,66μ	0,336	0,355	-5,39
42,6μ	0,5μ	30μ	0,66μ	0,308	0,297	3,68
42,6μ	0,5μ	40μ	0,66μ	0,280	0,256	9,26

It is possible to observe that the approach for the equivalent capacitance used in the model, presents accurate results, with relative errors inferior to 10% for most of the cases. Allowing to conclude that the approach presented above is a valid approximation.

By analyzing Eqns. (4.1) and (4.2) it is possible to conclude that a careful choice of the size of the load and switch transistors must be made. From one hand, increasing the size of the load transistors will increase the current along with the output frequency. Although, increasing the size of the load transistors will also increase the effective capacitance, which will decrease the frequency. The same balance happens with the switch transistors. From one side, increasing the size of the switch transistors will increase their speed of commuting. Although, increasing the size of the switch transistors will also increase the effective capacitance. Therefore, this balance has to be taken into account when sizing the load and switch transistors.

The existence of the above mentioned trade-offs among the several transistor sizes, leads to the conclusion that the design of Ring-VCOs is a good candidate for optimization based design.

In the next sub-section, several examples resulting from the optimization based design of Ring-VCOs will be presented.

### 4.3. Optimization of Ring VCOs

Once the model is fully designed and validated, it was included in an optimization-based script developed for the automatic design Ring VCO. This script enables the designer to obtain the transistors sizes for the delay cell of the ring VCO, for predefined values for the number of delay stages and the envisaged oscillation central frequency. The source for this script is included in Annex II. For the evaluation of the frequency vs control voltage characteristic, the equation (2.12) is used. For the evaluation of the currents, the EKV model with the parameters described in Chapter 3 were used. The evaluation of the effective Capacitance is obtained with (4.1).

The optimization of the oscillator consists in choosing a certain value of frequency, and fixing 2 of the 4 variables related to the length and width of both load and switch transistors. Notice that the sizes of the transistors were obtained for the central frequency with a control voltage of 0.6V. It is also clear, from Eqn. (4.2) that the frequency of operation cannot be the same for oscillators with 3, 5 and 7 stages. Thus, increasing the number of stages will limit the value of the maximum frequency possible to attain.

In the work example presented in this section, the sizes of the transistors were obtained for a frequency of operation of 0.5GHz for oscillators with 7 and 5 stages, and 1GHz for a 3 stage oscillator. The results of the optimization for these values of frequency concerning the size of the transistors are presented in the following Table 4.3.

**Table 4.3 Transistors sizes optimization**

$N$	$W_{load}$	$L_{load}$	$W_{sw}$	$L_{sw}$	$Freq_{estimated}$ [GHz]
3	30,2μ	0,39μ	78,9μ	0,39μ	1
5	57,9μ	0,39μ	63,6μ	0,66μ	0,5
7	80,0μ	0,39μ	71,4μ	0,40μ	0,5

Given the sizes of the transistors for each cell in each oscillator, a comparison was made between the values obtained from simulation against and the ones estimated from the model, concerning the frequency output, for a range of values for the control voltage between  $0.4V \leq V_c \leq 0.7V$ . The acquired results and its respective relative errors, related to the different oscillators, are presented in the following Tables 4.4, 4.5 and 4.6.

**Table 4.4-** Frequency estimated against frequency simulated for a 7 stage Ring VCO

$N$	$V_c$ [V]	$Freq_{estimated}$ [GHz]	$Freq_{simulated}$ [GHz]	$Relative\ Error$ [%]
<b>7</b>	0,4	0,887	0,818	-7,85
	0,45	0,790	0,708	-10,34
	0,5	0,693	0,638	-7,87
	0,55	0,595	0,589	-1,05
	0,6	0,499	0,498	-0,21
	0,65	0,405	0,422	4,31
	0,7	0,314	0,344	9,74

**Table 4.5-** Frequency estimated against frequency simulated for a 5 stage Ring VCO

$N$	$V_c$ [V]	$Freq_{estimated}$ [GHz]	$Freq_{simulated}$ [GHz]	$Relative\ Error$ [%]
<b>5</b>	0,4	0,89	0,785	-11,81
	0,45	0,792	0,720	-9,06
	0,5	0,694	0,663	-4,53
	0,55	0,597	0,585	-2,14
	0,6	0,50	0,511	2,14
	0,65	0,405	0,437	7,83
	0,7	0,315	0,357	13,55

**Table 4.6-** Frequency estimated against frequency simulated for a 3 stage Ring VCO

$N$	$V_c$ [V]	$Freq_{estimated}$ [GHz]	$Freq_{simulated}$ [GHz]	$Relative\ Error$ [%]
<b>3</b>	0,4	1,78	1,72	-3,28
	0,45	1,58	1,55	-1,91
	0,5	1,39	1,39	0,09
	0,55	1,19	1,21	1,32
	0,6	1,00	1,03	2,78
	0,65	8,11	8,53	5,16
	0,7	6,29	6,72	6,89

From the presented results, there are several conclusions possible to extract. The first conclusion relies on the small values for the relative errors, where the average error is inferior to 7%, making the optimization process and the model designed possible to be considered valid and accurate.

From the analysis of the results, it is also possible to observe that the relative error increases as the limits of the range of the control voltage are reached. The latter can be explained by the fact that the oscillator was designed with a value for the control voltage of  $0.6V$ , and by the fact that for values of the control voltage higher or lower than the range presented, the bias stage will not work properly.

Finally, as expected from Eqn. 4.2, the value of the operation frequency increases with the decrease of the control voltage and vice-versa.

In the next and final chapter, the conclusions extracted from this work will be presented.



## 5. Conclusions

### 5.1. Conclusions

In this thesis was analyzed a set of optimization techniques in the design of ring oscillators, using submicron technology, as well as a new model for characterizing the NMOs symmetric Load Ring VCO was presented.

After a brief introduction to the main VCO topologies, with the Ring Oscillator addressed in more detail, the particular case for Differential Ring VCOs with the Maneatis delay cell was taken in consideration, along with a careful analysis on the limitations of the models proposed in the literature when deep-submicron technologies are applied. Since the inaccuracy of the results obtained with the models presented stems from the inadequacy of using the MOS quadratic model to characterize the transistors with submicron sizes, the EKV model was considered. Results with this new model, for the working example presented related to the frequency response, prove the suitability of this new model.

The methodology adopted for the evaluation of the EKV model parameters was carefully described. A Matlab script for evaluating the EKV model parameters for both NMOs and PMOs transistors was developed, with functions based on the model equations, and the results obtained for UMC130 technology transistors were presented. The accuracy of the results were checked against simulation with Cadence Spectre through working examples considering the generation of the output characteristic of a switching inverter and the determination of delays for a chain of inverters. The results obtained, less than 7% of relative error between the outputs, guide us to the conclusion that the EKV model is adequate for the characterization of symmetrical-load ring VCOs.

Furthermore, an introduction to optimization-based design methodologies was made as well as the new model for characterizing the NMOs symmetric Load Ring VCO in submicron technologies was presented. In the Maneatis delay cell taken into consideration, the current source used grants an oscillator output signal swing equal to the control voltage. For the model to be valid, we must guarantee that the biasing current source remains in the saturation region, and that the switching transistors may be approximated to ideal switches. These considerations raise a limit to the maximum value of the control voltage that prevents the biasing transistors to enter the triode region of operation.

The approach for the equivalent capacitance used in the model was also presented. For the working example taken into consideration, the relative errors in the majority of the cases were inferior to 8%, which allow us to conclude that the approach used is a valid approximation.

The existence of trade-offs among the several transistor sizes, related to the frequency output and the effective capacitance, leads to the conclusion that the design of Ring-VCOs is a good candidate for optimization based design.

The validity of the VCO model for UMC130 Technology was tested against simulation results, as well as working examples considering the optimization based design of ring VCOs for oscillation frequencies up to 1.7 GHz were presented.

The average error inferior to 7% between the output frequencies, for the Ring VCOs presented for different stages and for different values of control voltage, makes the optimization process and the model designed valid.



## 5.2. Future Work

The ultimate objective of this work consists in developing optimization techniques in the design of ring oscillators in order to ensure a minimization of phase noise, and hence reduce the main disadvantage of this type of oscillators when compared to LC oscillators. To achieve such goal, an introduction of phase noise models as the main actor in the optimization process could be made, in order to minimize the phase noise.

In Chapter III, the EKV Model as well as the process for determination of the parameters for the UMC130 technology was presented. To perfect this process a fine tuned to some parameters could be made to further improve results.

Moreover, a future adaptation of the models developed for the Maneatis cell to other delay cells that allow the implementation of ring oscillators for higher frequencies, may provide an interesting challenge and results for this kind of oscillators.



## 6. Bibliography

1. Fino, M.H., *NMOS symmetric load ring VCOs modeling for submicron technologies*, in *VLSI Circuits and Systems II*. May 09, 2005, SPIE Proceedings: Sevilla, Spain.
2. Maneatis, J.G., *Low-Jitter Process-Independent DLL and PLL Based on Self-Biased Techniques*. IEEE Journal of Solid State Circuits. **31**: p. 1723-1732.
3. Toifl, T., *Integrated Circuits for the Synchronization of High-Energy Physics Experiments*. 1999, Technische Universitat Wien: Austria.
4. M.H. Fino, A.B.L., *Accurate Modeling of Submicron Symmetric Load Ring VCOs*, in *IEEE International Conference on Electronic Design*. 2004. p. 1024-1.
5. Fino, M.H., *Accurate Modeling of Submicron CMOS Ring Voltage Controlled Oscillators*, in *IEEE ICM'07*. Cairo, Egypt.
6. Coito, M.H.F.a.F.V., *Symbolic Characterization of VCOs and its Application to Optimization Based Design*, in *Design of Analog Circuits through Symbolic Analysis*, E.T.-C.a.F.V.F. Mourad Fakhfakh, Editor. 2010, Bentham Science Publishers Ltd. p. 399-412 (14).
7. Sarkar, M.K.M.B.C., *Ring Oscillators: Characteristics and applications*. Indian Journal of Pure & Applied Physics, February 2010. **48**: p. 136-145.
8. G. Jovanović, M.S.c., Z. Stamenkovic *A CMOS Voltage Controlled Ring Oscillator with Improved Frequency Stability*. 2010. **vol. 2, 1**.
9. Fino, M.H., *Accurate Modeling of Submicron CMOS Ring Voltage Controlled Oscillators*, in *2007 International Conference on Microelectronics*. Dec. 2007, IEEE Publishing. p. pp.97-100.
10. Vittoz, C.C.E.a.E.A., *CMOS Low-Power Analog Circuit Design*, in *Emerging Technologies*. 1998, IEEE.
11. Christian C. Enz, F.K.a.E.A.V., *An Analytical MOS Transistor Model Valid in All Regions of Operation and Dedicated to Low-Voltage and Low-Current Applications*. Analog Integrated Circuits and Signal Processing, 1995.
12. Stefanović, D. and M. Kayal, *Structured analog CMOS design*, in *Analog circuits and signal processing*. 2008, Springer,: Dordrecht ; London. p. xii, 283 p. ill. 25 cm.
13. Brinson, M., *Verilog-A implementation of the EKV v2.6 long and short channel MOSFET models*. 2008, Qucs.
14. Matthias Bucher, C.L.a.C.C.E., *An Efficient Parameter Extraction Methodology for the EKV MOST Model*, in *Proc. 1996 IEEE Int. Conference on Microelectronic Test Structures*, E.L. Swiss Federal Institute of Technology (EPFL), ELB-Ecublens, Editor. 1996: Trento, Italy.



## Annex I

```
close all, clc

% Import data from Cadence to structure plotData
plotData=importdata('File1');

% Export data from structure to each one of the variables
xdata=plotData.data(:,1);
Id=plotData.data(:,2);

plot(xdata,Id)

% Value for Vt
Vt=0.02585;

root_Id=sqrt(Id);

% Function to fit
F = @(x,xdata)x(1)*xdata + x(2);

% initial values for the parameters
x0=[1 1];

% fitting the data
options=optimset('TolF',1e-27,'TolX',1e-27);
x=lsqcurvefit(F,x0,xdata,root_Id,[],[],options);

figure(2)
plot(xdata,root_Id);

figure(3)
plot(xdata, F(x,xdata))
hold on
plot(xdata,root_Id,'r')

% Calculating the slope and Ispecific
slope=abs(x(1))
Is=(slope^2)*4*(Vt^2)

close all, clc, clear all

% Import data from Cadence to structure plotData
plotData=importdata('File2');

% Export data from structure to each one of the variables
Vg=plotData.data(:,1);
Vpp=plotData.data(:,2);

% Values
Vto=0.1875;
Is=2.33e-6;
```

```

%Parameters UMC130 technology
Eox=3.453e-11;
Esi=1.045e-10;
tox_n=2.73e-9;
tox_p=2.86e-9;

Cox_n=Eox/tox_n;
Cox_p=Eox/tox_p;

figure(1)
plot(Vg,Vpp)

% %Function to fit (in order to obtain n)
F = @(x,Vg)Vg-Vto+x(2).*sqrt(x(1))-x(2).*(sqrt(Vg-Vto+x(1)+x(2).*sqrt(x(1)))+(x(2)./2).^2)-
(x(2)./2));
%
% %initial values for the parameters
x0=[1 1];
%
% %fitting the data
options=optimset('TolF',1e-27,'TolX',1e-27);
x=lsqcurvefit(F,x0,Vg,Vpp,[],[],options);
%
fi=x(1)
gama=x(2)

VGprime=Vg-Vto+fi+gama*sqrt(fi);

Vp=VGprime-fi-gama*(sqrt(VGprime+(gama/2)*(gama/2))-(gama/2));

n=(1-gama./(2.*(sqrt(Vp+fi))))).^-1;

for i=1:length(Vg)
    if Vg(i)==1.152
        n2=n(i);
    end
end

clc, close all

%Import data from Cadence to structure plotData
plotData=importdata('File3');

%Export data from structure to each one of the variables
VgW=plotData.data(:,1);
VpW=plotData.data(:,2);

gama_linha=[];

Vto=0.1875;
gama=0.209;
fi=0.7234;

Lmin=120e-9;
Wmin=160e-9;

```

```

DL=0.5*Lmin;
DW=0.5*Wmin;

% Transistor Dimensions
W2=50e-6;
W=1e-6;
L=0.39e-6;
L2=10e-6;

figure(1)
plot(VgW,VpW,'g')

Vgprim=VgW-Vto+fi+gama*sqrt(fi);

syms gamaL

for i=1:length(VgW)
    gama_li=solve(VpW(i)-Vgprim(i)+fi+gamaL*(sqrt(Vgprim(i)+((gamaL/2)^2))-
(gamaL/2)),gamaL);
    gama_linha(i)=double(gama_li);
end

gama_linhax=gama_linha';

z1=Esi*Eox/(Cox_n*1e-12);
z2=sqrt(fi+VgW);
z3=W-DL;
z4=sqrt(fi+VpW);

F= @(x,VgW)z1.*(3.*x(1)/z3).*z4;

% initial values for the parameters
x0=[1e-1];

% fitting the data
options=optimset('TolF',1e-27,'TolX',1e-27);

lb = 0.0;
ub = gama;

x=lsqcurvefit(F,x0,VgW,(gama_linhax-gama),[],[],options);

weta=x(1)

gamaWLinha=gama+z1*(3.*weta/z3).*z4;

VpW=Vgprim-fi-gamaWLinha.*(sqrt(Vgprim+(gamaWLinha/2).^2)-gamaWLinha/2);

close all, clc, clear all

graf=importdata('File4');

% Export data from structure to each one of the variables
Vg=graf.data(:,1);

```

```

Ids=graf.data(:,2);

Kn=500e-6;

Lmin=120e-9;
Wmin=160e-9;

%Nmos Parameters
Weta=0.344;
Leta=0.0351;

W=50e-6;
L=10e-6;

z1=Esi*Eox/(Cox_n*1e-12);

z3=Leta/(L-DL);

VGprime=Vg-Vto+fi+gama*sqrt(fi);

Vp=VGprime-fi-gama*(sqrt(VGprime+(gama/2)*(gama/2))-(gama/2));

n=(1-gama./(2.*(sqrt(Vp+fi+4*Vt)))).^-1;

% %Function to fit (in order to obtain n)
F = @(x,Vg)(n./2).*(Vp.^2).*Kn.*(W/L).*(1./(1+x(1).*Vp));
%
% %initial values for the parameters
x0=[1];
%
% %fitting the data
options=optimset('TolF',1e-27,'TolX',1e-27);
x=lsqcurvefit(F,x0,Vg,Ids,[],[],options);

Ids1=(n./2).*(Vp.^2).*Kn.*(W/L).*(1./(1+x(1).*Vp));

figure(2)
plot(Vg,Ids)
hold on
plot(Vg,Ids1,'r')

theta=x(1)
beta=Kn*(W/L).*(1./(1+theta.*Vp))

```



## Annex II

```
function [ output_args ] = Opt_Ws( input_args )

close all, clc, clear all

%Parameters UMC130 technology
Eox=3.453e-11;
Esi=1.045e-10;
tox_n=2.73e-9;
tox_p=2.86e-9;

q=1.602e-19;

Cox_n=Eox./tox_n;
Cox_p=Eox./tox_p;

Lmin=120e-9;
Wmin=160e-9;

DL=0.5*Lmin;
DW=0.5*Wmin;

global Vt fi_n gama_n Vto_n Weta_n Leta_n z1_n z3_n Kn W_n L_n theta_n fi_p gama_p
Vto_p Weta_p Leta_p z1_p z3_p beta_p theta_p Kp

Vt=0.02585;

%Nmos Parameters
fi_n=0.7234;
gama_n=0.209;
Vto_n=0.1875;
Kn=500e-6;
theta_n=0.9765;
Weta_n=0.344;
Leta_n=0.0351;

W_n=40e-6;
L_n=0.39e-6;

z1_n=Esi*Eox/(Cox_n*1e-12);

z3_n=Leta_n/(L_n-DL);

%Pmos Parameters
fi_p=1.4088;
gama_p=0.4594;
Vto_p=0.2508;
Weta_p=0.0869;
Leta_p=0.0083;
Kp=100e-6;
theta_p=0.25;
```

```

W_p=10e-6;
L_p=0.39e-6;

z1_p=Esi*Eox/(Cox_p*1e-12);

%z3_p=Leta_p/(L_p-DL);

function beta=getBeta(Vp,mos)

    if mos
        beta=Kn.*(W_n/L_n).*(1./(1+theta_n.*Vp));
    else
        beta=Kp.*(W_p/L_p).*(1./(1+theta_p.*Vp));
    end

end

function is2=getIspec(Vp,mos)

    if mos
        n_n=getN(Vp,mos);
        beta_n=getBeta(Vp,mos);
        is2=2.*n_n.*beta_n.*Vt^2;
    else
        n_p=getN(Vp,mos);
        beta_p=getBeta(Vp,mos);
        is2=2.*n_p.*beta_p.*Vt^2;
    end

end

function i=getI(Vp,Vx)

    i=(log(1+exp((Vp-Vx)/(2*Vt)))).^2;

end

function g=getGamaLinha(Vd,Vs,mos)

    if mos
        g=gama_n-z1_n.*(z3.*sqrt(fi_n+Vd)+(z3_n-(3*Weta_n/(W_n-DW))).*sqrt(fi_n+Vs));
    else
        g=gama_p-z1_p.*(z3_p.*sqrt(fi_p+Vd)+(z3_p-(3*Weta_p/(W_p-DW))).*sqrt(fi_p+Vs));
    end

end

function n=getN(Vp,mos)

    if mos
        n=(1-gama_n./(2.*(sqrt(Vp+fi_n)))).^-1;
    else
        n=(1-gama_p./(2.*(sqrt(Vp+fi_p)))).^-1;
    end

end

function vp=getVp(Vg,mos)

```

```

if mos
    %gamaL_n=getGamaLinha(1.2,0);

    gamaL_n=gama_n;

    Vgprim_n=Vg-Vto_n+fi_n+gama_n*sqrt(fi_n);

    vp=Vgprim_n-fi_n-gamaL_n.*(sqrt(Vgprim_n+(gamaL_n/2).^2)-gamaL_n/2);
else
    %gamaL_p=getGamaLinha(Vg,0,0);

    gamaL_p=gama_p;

    Vgprim_p=Vg-Vto_p+fi_p+gama_p*sqrt(fi_p);

    vp=Vgprim_p-fi_p-gamaL_p.*(sqrt(Vgprim_p+(gamaL_p/2).^2)-gamaL_p/2);
end

end

function y=id(Vdx,Vgx,Vsx,mos)

Vp=getVp(Vgx,mos);
ifl=getI(Vp,Vsx);
ir=getI(Vp,Vdx);
Ispec=getIspec(Vp,mos);

y=Ispec.*(ifl-ir);

end

function f=myfun(x)

Freq=0.5e9;
K=0.7;
N=7;
Vc=0.6;

Vp_p=getVp(Vc,0);
ifl_p=getI(Vp_p,0);
ir_p=getI(Vp_p,0.6);
n_p=getN(Vp_p,0);

dif=(ifl_p-ir_p);

Ceff_aux1=Cox_n*K*L_n;
Ceff_aux2=Cox_p*K*L_p;
aux_p=2.*n_p*Kp.*(1./(1+theta_p.*Vp_p)).*Vt^2;

AUX=aux_p*dif;

correc=(tan(pi/N)/(pi/N));

AUX2=N*Vc;

```

```

f=abs(Freq-((AUX.*(x(1)./L_p))./(AUX2.*(Ceff_aux1*x(2)+Ceff_aux2.*x(1))))*correc);

    end

    %%% Opt W_load and W_sw with fmincon %%%

    x0=[1e-6;1e-6];

    lb=[1e-6; 1e-6];
    ub=[80e-6; 80e-6];

    options = optimset('Algorithm','sqp','TolF',1e-23,'TolX',1e-
23,'MaxIter',1e5,'MaxFunEvals',1e4);

    [x,fval,exitflag]=fmincon(@myfun,x0,[],[],[],[],lb,ub,[],options);

    W_load=x(1)
    W_sw=x(2)

    end

```

